ARTICLE

OPEN

Check for updates

Formation of the eclogites of the Atbashi complex, Kyrgyzstan, in a subduction zone mélange diapir

Miao Sang[1,2,3], Zhou Tan[1,2,3✉], Wenjiao Xiao[1,2,3,4✉], Qigui Mao[1,2,3], Hao Wang[1,2,3], Rui Li[1,2,3] & Qingqing Qiao[1,2,3]

Much debate exists concerning mechanisms of crustal material transfer from subducting slab to overlying mantle. Formation of mélange rocks by physical mixing of slab components within subduction plate interface is predicted to transfer their compositional signal to source of arc magmas by ascending as diapirs from slab-top. Despite being supported conceptually and through modeling, existence of these diapirs in global subduction architecture remains inconclusive. Here we use petrological observations, thermometry and thermodynamic modeling, combined with geochemical constraints and compilation of massive existing data, to investigate eclogites from a deeply buried mélange "package" in Kyrgyz Tianshan, southern Altaids. We find that various slab components physically mixed to form eclogitic mélange rocks at threshold depth of the subarc (i.e., ≥85 km). Index mineralogical and Pressure-Temperature records indicate a thermal history with substantial heating after peak burial to condition crossing wet solidus. Such translation, toward hot corner of mantle wedge, is short-lived around several hundred thousand to few million years, serving as first tangible evidence substantiating mélange diapirs propagate and dynamically mix with overlying mantle. Contemporaneous Late Carboniferous flare-up of regional arc magmatism with mélange diapir melting signal also advocates that non-negligible process of mantle wedge hybridization by buoyant mélange materials, to transfer volatile, generate arc lavas and regulate terrestrial geochemical cycles, stands.

[1] National Key Laboratory of Ecological Safety and Sustainable Development in Arid Lands, Xinjiang Institute of Ecology and Geography, Chinese Academy of Sciences, Urumqi 830011, China. [2] Research Centre for Mineral Resources, Xinjiang Institute of Ecology and Geography, Chinese Academy of Sciences, Urumqi 830011, China. [3] Innovation Academy for Earth Science, Chinese Academy of Sciences, Beijing 100029, China. [4] College of Earth and Planetary Sciences, University of Chinese Academy of Sciences, Beijing 100049, China. ✉email: tanzhou@ms.xjb.ac.cn; wj-xiao@mail.iggcas.ac.cn

G aining insight into the seismic and volcanic eruptions that occur in arc formations necessitates a comprehensive knowledge of the mechanisms responsible for the movement of material between the mantle wedge and subducted slab in subduction zones. In particular, the transfer of volatile from Earth's surface to the deep mantle are largely controlled by those processes with vital implications for plate tectonics[1], long-term global climate[2], and the evolution of Earth's heat budget[3]. Nonetheless, the transport mechanisms in which slab material is moved into the mantle wedge is widely disputed[4–9], lead to an unclear awareness of global volatile cycling. Besides, the mechanism of fluid flow propagation (i.e., pervasive *versus* channelized[10–12]) and the fact of Phanerozoic secular cooling of Earth mantle[13] also hinder the efficiency of volatile mobilization beneath the subarc, further making the feeding of subducted volatile into the mantle wedge remains ambiguous[14]. Flawed conclusions regarding both the long-term evolution of the crust and mantle, as well as the short-term recycling of volatiles shall raise, if geodynamic models used to assess geochemical and geophysical data related to subduction zones are of questionable accuracy.

Direct geophysical observations of subarc processes, however, presently lack the resolution to obtain fine-scale information about the material transfer processes at the slab-mantle interface. The chemical and isotopic compositions of arc lavas offer chance to extract critical information from the key regime of subduction zones (e.g., the subarc).

Research conducted over the past decade has demonstrated that a combination of partial melting of subducted sediments and metamorphic dehydration of altered oceanic crust (AOC) is capable of producing the required trace element fractionations (e.g., Nb-Ta negative anomaly, LILEs enrichment, and HFSEs depletion)[7,15,16]. Consequently, a metasomatized mantle model (e.g., refs. [17,18]) is applied by most studies of subduction zone processes as the primary vector to explain material transfer between the descent slab and overlaying mantle wedge, with a common trait that the diagnostic trace element fractionation of arc lavas is produced in the slab before mixing with the mantle wedge takes place[5,19]. However challenges have raised, from experimental petrology, in simultaneously reproducing both major and trace element features of the most common types of arc magmas (i.e., tholeiites and calc-alkaline melts)[20]. Furthermore, argument has been recently proposed, for the debate of the processes by which typical trace element signatures are bred to arc magmatism, that the trace element and isotope variability of the magmas of global arc could not be simply settled with the classic model which introduces a hybridized mantle wedge by discrete feedings of fluids and/or aqueous melts from slab components[9,19]. Instead, reconciliation can only be achieved if physical mixing of depleted mantle (DM), AOC, and sediments arises early within the plate interface during subduction prior to any melting takes place[5]. The order of events is thus redefined, as a prerequisite, to back up the fundamental role of mélange for the genesis of arc magmatism. Laboratory[21] and numerical modelings[22–25] of subduction process have revealed that gravitational instabilities could be produced by hydration and partial melting at the slab-mantle interface, with further development into diapiric structures composed of partially molten materials[20]. Yet these diapirs have not been unambiguously imaged and accepted in global subduction zone architecture, probably due to the following reasons: (1) Along arc geophysical studies are rare, and the current resolution of seismic techniques may not be appropriate to image mixed mélange-peridotite lithologies; (2) Magnetotelluric approach, sensitive to interconnected free fluids, would not easily detect the presence of mélanges, where most of the water may be crystallographically bounded. It is also not able

to detect the difference between fluids generated by a dehydrating mélange diapir and those released at the slab-top, which percolate the mantle wedge; (3) Several km-thick low-seismic velocity regions observed at the slab-top in subduction zones worldwide indicate the persistence of mélange zones (mainly hydrated rocks and sediments) in the slab-mantle interface[26–28]. Field evidence reveals multiple mélange outcrops worldwide (see refs. [5,29] for comprehensive review) but voluminous deeply burial and exhumation of sediments is of scarcity (10–15 km, Apennines, Italy[30]; 50–60 km, Raspas complex, Ecuador[31]), especially for those exhumed from subarc depths (i.e., ~85–140 km, >2.6 GPa[12]). This, in turns, obstructs direct evaluation of the degree of chemical and/or mechanical disruption of subducted material along the plate interface.

Here we present a comprehensive study on eclogites with distinct pressure-temperature-protolith histories from a deeply buried mélange "package" in the Atbashi low-temperature (LT)-high-pressure (HP) metamorphic complex, Kyrgyzstan section of the South Tianshan Metamorphic Complex (STMC), southern Altaids (Fig. 1). Recent studies[32,33] in the Chinese section of the STMC disclose massive sediment accretion at ~80 km depth along the subduction interface, suggesting continuous refrigeration, by incoming cold material from the slab, and juxtaposition to the "cold nose" of mantle wedge. In addition, transient thermal excursion was revealed, in region, from strikingly concordant chemical zonation of garnet in coesite-bearing oceanic eclogites[34], disclosing the potential translation of ultra-high-pressure rocks (UHP) refrigerated slices near to a relatively hotter mantle wedge. In this study, field mapping, bulk-rock geochemistry, metamorphic petrology, Zr-in-rutile & Ti-in-quartz thermobarometers, thermodynamic modeling, rutile & zircon trace elements, and U-Pb chronology analyses have been conducted to provide the first tangible eclogitic rock evidence recording mélange diapir melting signal (MDP) and experiencing substantial thermal excursion in a well-preserved refrigerated subduction plate interface, as confirmed by the pervasive presence of low-temperature eclogitic rocks (refs. [33,35–40] and also this study). Additional multi-disciplinary data, especially those Late Carboniferous ones, are also compiled from regional various lithologies to fingerprint the temporal-spatial variations of mantle signal and crustal feedback during which the eclogitic mélange rocks contemporaneously formed and their fate during substantial thermal excursion. Available data provide insights into a model of mélange diapir melting in refrigerated subduction plate interface as substantiated in the STMC. Implications for such process with a momentous contribution in transferring crustal volatile from slab surface to arc lava, regulating terrestrial geochemical cycle, are thus discussed.

Results
The Kembel mélange in the Atbashi metamorphic complex. The construction of the Altaids involves the welding of the North China, Alxa, Karakum-Tarim, Siberia, and East European cratons (Fig. 1)[41,42]. The 2500 km-long South Tianshan Orogenic Belt (STOB, see Supplementary Note 1 for detailed geological background in Supplementary Information), is located in the southern Altaids, extending from the western deserts of Uzbekistan, Tajikistan, Kyrgyzstan, and Kazakhstan to northern Xinjiang in China, and formed in response to the final amalgamation between the Tarim and Siberian cratons[43–45]. The STOB is comprised of the Kazakhstan-Yili-Central Tianshan Continent (KYCTC) in the north and South Tianshan accretionary complex (AC, including the South Tianshan Belt, STB) in the south, and is bounded to the south by the North Tarim Fault (NTF) with the North Tarim Craton[46,47]. The Atbashi metamorphic complex (ATMC)
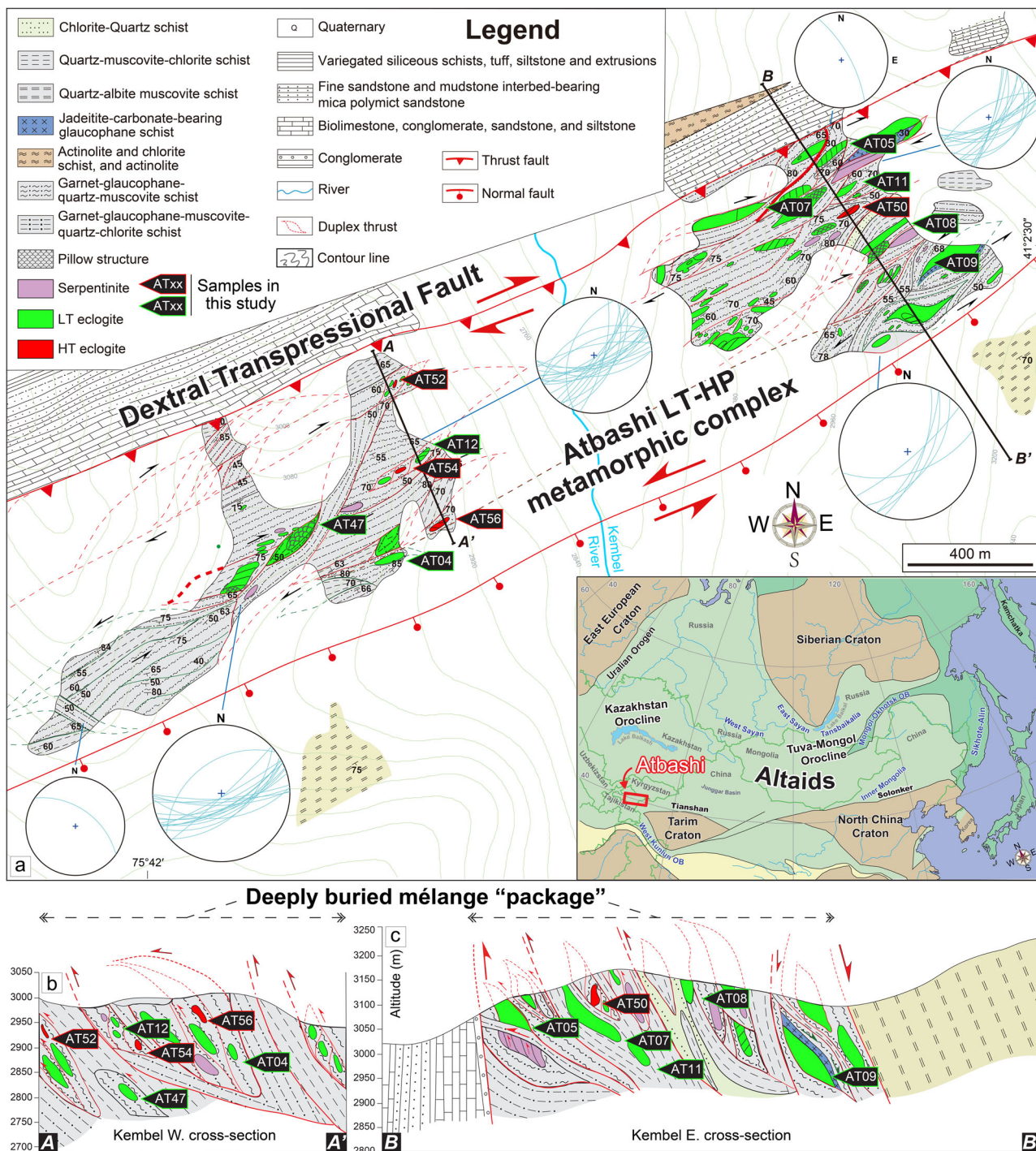
Fig. 1 The Kembel mélange in the Atbashi range of the STOB. a Location of the research area and geological map with close-up view showing the regional geological setting and sampling location (modified after ref. [52]). **b, c** Two cross-sections constructed, along the Kembel valley, across the Atbashi HP/UHP mélange with key structural elements and detailed sample sites.

represents the central part of the South Tianshan LT-(U)HP metamorphic complexes (STMC) within the southern Altaids and extends for about 120 km along the Atbashi-Inylchek-South Central Tianshan Fault and correlates with the Akeyazi[33,37], Chatkal[48,49] and Fan-Karategin[50] (U)HP metamorphic complexes, which crop out in China, Kyrgyzstan and Tajikistan segments of the STOB, respectively. Numerous previous studies[32,33,35,36,48,51] focused on the P-T-isotopic ages history of high-grade metamorphized lithologies had confirmed the existence of a refrigerated subduction plate interface during the

recovery of the STMC (500–600 °C, 2.0–3.0 GPa, Fig. 1). Our studied area, named as the Kembel mélange[51–54], lies close to the north boundary of the ATMC and is clamped in between the North and South regional greenschist-facies units. It was crosscut by the Kembel River as a ~1 km wide N-S across, deeply buried mélange "package" (Fig. 1b, c) predominantly composed of strongly schistose, high-grade metamorphosed, meta-volcanoclastics hosting eclogitie-/blueschist-facies mafic meta-volcanics, as well as serpentinite, as pods, lenses, boudins, thin layers or massive blocks and marble horizons (Fig. 2).
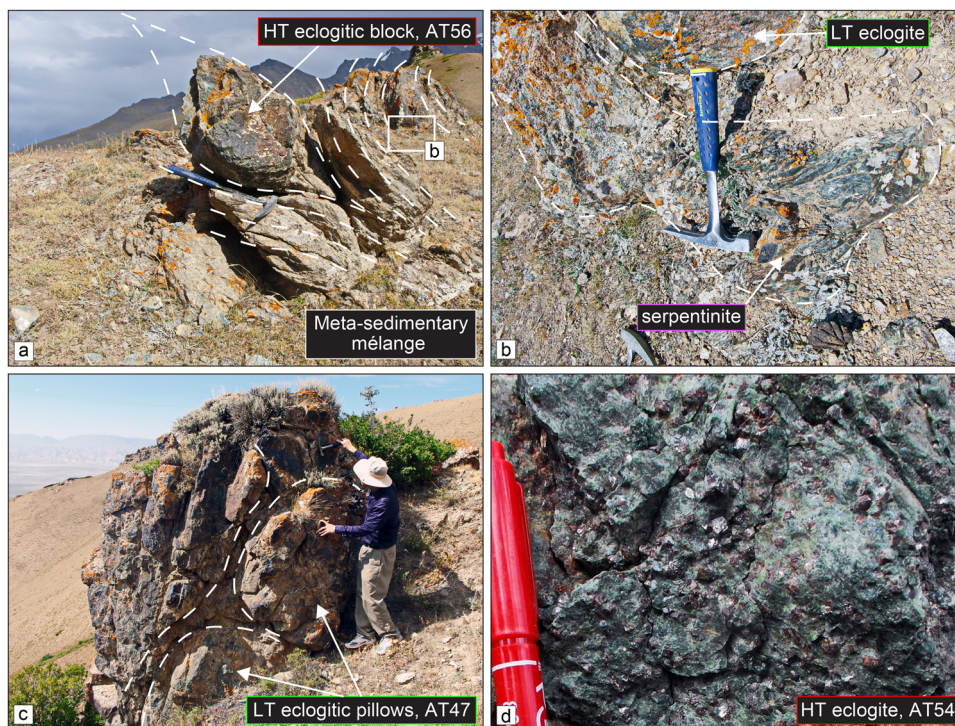
Fig. 2 Outcrop features. a, b Outcrop observation of representative HT and LT eclogites wrapped within meta-sedimentary mélange. **c** Figure shows LT eclogitic pillows. **d** Representative outcrop of HT eclogite with contrasting bottle green color.

Sampling strategy. To determine the petrogenesis, as well as the protolith and metamorphic ages, of eclogitic blocks (their contrasting features are described in the following context) wrapped within the Kembel mélange, twenty samples were collected, including four HT and eight LT eclogites (highlighted with red and green boxes/colors in Fig. 2 and following figures, respectively, Supplementary Data 1), several serpentinite blocks and meta-volcanoclastic host rocks were sampled (Fig. 2), on outcrops along the Kembel West and East cross-sections, for petrographic, mineralogical, and geochemical investigation. Of these, representative samples of HT and LT eclogites were selected for bulk-rock geochemistry (major and trace element and Sr-Nd isotopic composition, Supplementary Data 3, 4), rutile and quartz trace element composition (Supplementary Data 5, 6), and rutile, as well as zircon, U-Pb isotopic chronology analysis (Supplementary Data 7–9).

Petrography, petrology, and P-T estimates. Two types of eclogites (Supplementary Data 1) were recognized by color on a hand-sample scale: one has a bottle-green and the other a pale-green appearance (Figs. 2, 3, Supplementary Fig. 1). The bottle green eclogite (i.e., HT one, Fig. 3a, Supplementary Fig. 1a–c) is comprised of moderate size pink garnet porphyroblast (1–2 mm in diameter) and coarse-grained grass green clinopyroxene matrix (50–100 μm) painted with massive irregular patches of quartz (Fig. 3a–c, Supplementary Figs. 1a–c, 2) and opaque ilmenite (with few relic rutile) as well as minor dark-blue amphibole and phengite. Some pseudomorphs[55], as "nano-diorite" inclusions with 100–200 μm size in garnet, after films of melt (Supplementary Fig. 2g, h) were identified with a fine-grained aggregate of quartz + clinopyroxene ± ilmenite ± epidote, yet no glassy was present. Orthopyroxene, despite predicted to be stable during decompression (Supplementary Fig. 8c), was not detected too, likely due to the potential limited inconsistency between the chosen bulk composition and artifacts of the solution models used to estimate mineral assemblages. In contrast, the pale-green

eclogite (i.e., LT one, Fig. 3d, Supplementary Fig. 1d–f) is filled with fine-grained pink-white garnet porphyroblast (0.2–0.6 mm) and grayish green clinopyroxene matrix (20–50 μm) associated with minor blue amphibole, phengite, paragonite and rutile armored by titanite. Epidote is mainly present, as retrograde phase after lawsonite breakdown, in the pale-green eclogite (i.e., LT one, Supplementary Fig. 1d, e).

Mineral chemistry analysis (Supplementary Fig. 3b, e, Supplementary Data 2) discloses that garnet in HT eclogite is generally enriched in Mg (i.e., X_{pyrope} ~0.14–0.18) but depleted in Fe and Ca (i.e., $X_{almandine}$ ~0.65–0.72 and $X_{grossular}$ ~0.12–0.19), compared to that in LT eclogite (X_{pyrope} ~0.04–0.08, $X_{almandine}$ ~0.68–0.78 and $X_{grossular}$ ~0.18–0.21); In addition, clinopyroxene in HT eclogite is principally of diopside-aegirine-augite ($X_{jadeite}$ ~0.21–0.26, $X_{diopside}$ ~0.52–0.56 and $X_{aegirine-augite}$ ~0.18–0.26), countering to that from LT one ($X_{jadeite}$ ~0.42–0.52, $X_{diopside}$ ~0.42–0.47 and $X_{aegirine-augite}$ ~0.04–0.15); Besides, amphibole in HT eclogite displays solid-solution composition of winchite-barroisite while that from LT one falls within the range of glaucophane-barroisite; White mica in both HT and LT eclogites are mainly phengite (Si^{4+} ~3.32–3.50 a.p.f.u.); Contrasting Zr content (~600–750 *versus* ~20–35 μg g^{-1}, Fig. 4a, Supplementary Fig. 4, Supplementary Data 5), which may be temperature dependent[56], characterizes rutile from HT and LT eclogites. Besides, Ti-in-quartz solubility was evaluated, ranging from 2 to 5 μg g^{-1} (Fig. 4a, Supplementary Fig. 5, Supplementary Data 6), as a thermobarometer in combination with Zr-in-rutile thermometer and independent P-T estimates via thermodynamic modeling.

Rutile in HT eclogite records temperature of 808 ± 15 °C ($n = 72$, with calibration of ref. [57]), while in LT eclogite, the temperature is averaged at 555 ± 18 °C ($n = 49$). None of correlation, between recorded Zr-in-rutile temperatures and the presence or absence of garnet armoring (820 ± 9.3 °C *versus* 814 ± 9.1 °C, Supplementary Data 5), is observed (Supplementary Fig. 4a). Such a HT condition is also echoed by temperature
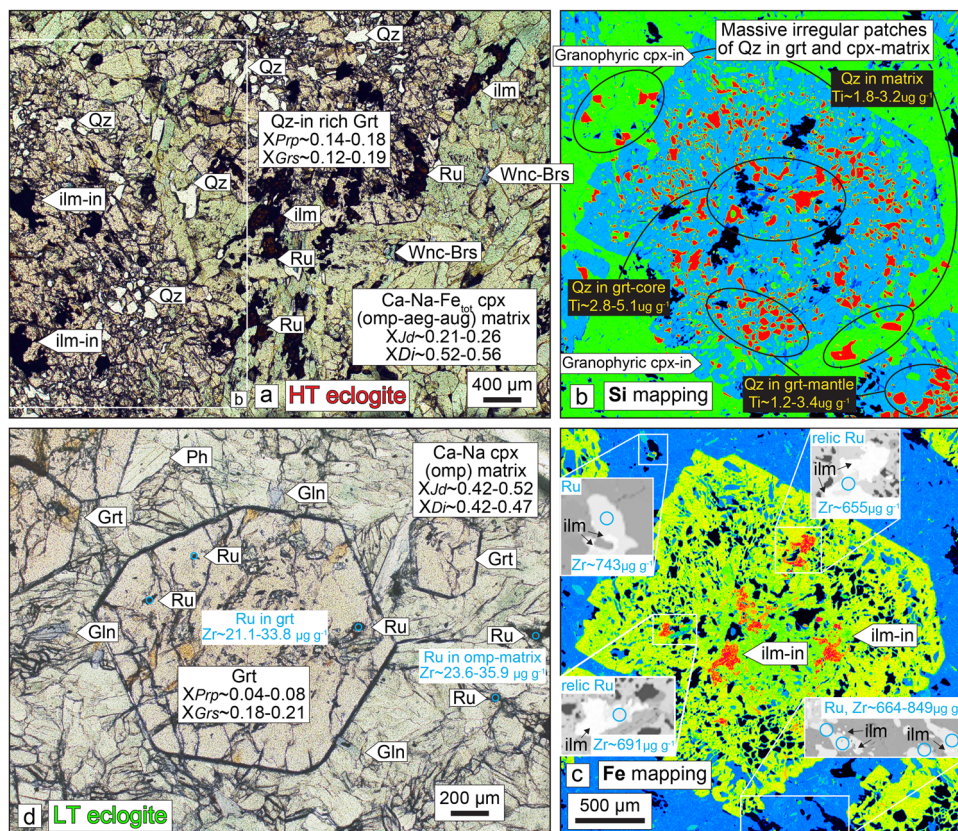
Fig. 3 Distinct petrological features. a Representative petrography of HT eclogite on microscope scale; more detail is presented in Supplementary Fig. 1 in Supplementary Information. **b, c** Si and Fe microprobe mapping show the localities of key minerals (i.e., quartz and ilmenite) and massive irregular patches of quartz inclusions in the garnet porphyroblast of HT eclogites; measurements of Ti-in-quartz and Zr-in-rutile are highlighted; see Supplementary Fig. 2 for corresponding BSE image and microprobe Mn, Ca, Mg elemental mapping. **d** Petrographical feature of LT eclogite on microscope scale.
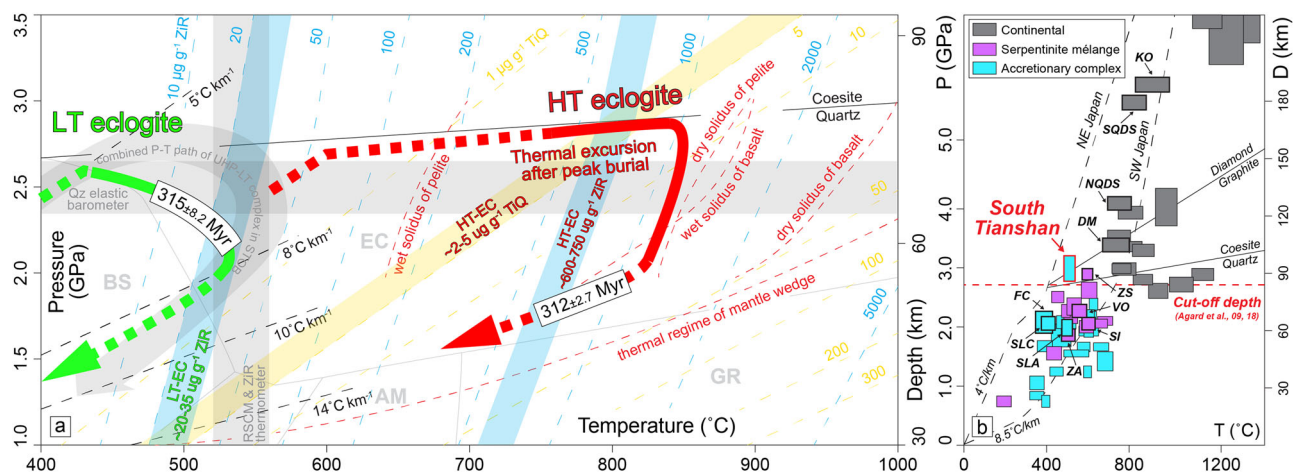

Fig. 4 Contrasting P-T histories. a Summary of P-T-time histories of studied eclogites; age constraints are from SIMS rutile U-Pb chronology in Supplementary Fig. 7; red and green trajectories are mainly derived from thermodynamic modeling with mineral compositional constraints (Supplementary Figs. 8 and 9); isopleth of Ti-in-quartz and Zr-in-rutile are plotted via calibrations of refs. [57,132] with pressure set to 2.7 GPa; solidus of various compositions are cited from thermodynamic modeling[145,149] and experimental petrology[150,151]; comprehensive reviews[32,33,35,36,74] of the P-T estimates, via thermodynamic modeling, quartz elastic barometer, and RSCM & Zr-in-rutile thermometers, of the STMC, which suggests a deep refrigerated condition (i.e., ~2.5 GPa, 540 °C), are also plotted for comparison. **b** P-T characteristics of the STMC compared to the global compilation[30,58]; worldwide representative fossil subduction suture zone is marked by bold text & rectangle; KO Kokchetav, SQD South Qinling-Dabie, China; NQDS North Qinling-Dabie-Sulu, China; DM Dora Maira, Italy; ZS Zermatt, Switzerland; VO Voltri, Italy; FC Franciscan C., California; SI Sistan, Iran; SLC Schistes Lustrés, Corsica; SLA Schistes Lustrés, Western Alps; ZA Zagros, Iran. Coesite-Quartz transformation follows the one that ref. [152] calibrated experimentally.

estimate ~791 ± 38 °C by Ti-in-quartz thermobarometer with pressure set to 2.7 GPa ($n = 69$, Fig. 4a, Supplementary Data 6). P-T evolution of HT eclogites, as constrained by pesudosection modeling and chemical zonation of key minerals (Supplementary Figs. 8, 9), is characterized by near isobaric burial with substantial heating from 720, 2.6 to 820 °C, 2.7 GPa, and subsequently isothermally decompressing, crossing the wet solidus (Fig. 4a, Supplementary Fig. 8c), to 805 °C, 2.0 GPa. By comparison, LT eclogite experiences slightly decompression with heating from 450 °C, 2.6 GPa to its peak metamorphism at 530 °C, 2.2 GPa (Fig. 4a, Supplementary Fig. 9). P-T characteristics of the STMC (Fig. 4b) is also compared to the global compilation[30,58].

Bulk-rock geochemistry. Bulk-rock major and trace elements, as well as Sr-Nd isotopes, analysis (Supplementary Data 3, 4) were conducted to investigate the protolith nature of studied eclogites. Both HT and LT eclogites are substantially of basaltic composition, but the latter is more mafic (Supplementary Fig. 6a) with different SiO_2 (~52 versus ~44 wt %), CaO and FeO_{tot} but comparable MgO and Al_2O_3 concentrations. HT eclogites show broadly positive slope in LREEs to MREEs and flat in HREEs, with $(La/Sm)_N$ ~1.59–3.46 and $(Gd/Yb)_N$ ~0.94–1.576, as well as $(^{86}Sr/^{87}Sr)_i$ ~0.703923–0.707086 and $(^{143}Nd/^{144}Nd)_i$ ~0.512352–0.512488 isotopic compositions. By contrast, patterns of depleted LREEs-MREEs and horizontal HREEs $((La/Sm)_N$ ~0.28–1.43, $(Gd/Yb)_N$ ~0.7–1.05) are tied to LT eclogites with ~0.702494–0.705392 and ~0.512370–0.512678 in $(^{86}Sr/^{87}Sr)_i$ and $(^{143}Nd/^{144}Nd)_i$ ratios, respectively.

Rutile and zircon U-Pb isotopes. Forty-seven and twenty-three rutile grains, with diameters about 75.3 ± 20.0 and 136 ± 57.0 µm (Supplementary Fig. 4a, b), from two HT and LT eclogites, respectively, were analyzed (Supplementary Data 9). The measured U contents of all rutiles range from 0.05 to 4.1, mostly <1 µg g^{-1} with f_{206} values of common lead between 1 and 88%. On the Tera-Wasserburg linear regression plot, HT eclogites (AT54 and 50, Supplementary Fig. 7a, b) yield lower intercept ages of 312 ± 2.7 Myr (with upper intercept at $^{207}Pb/^{206}Pb = 0.86 ± 0.03$, MSWD = 1.0, $n = 26$) and 313 ± 7.4 Myr (with upper intercept at $^{207}Pb/^{206}Pb = 0.96 ± 0.04$, MSWD = 2.1, $n = 21$), broadly consistent with their weighted mean $^{206}Pb/^{238}U$ ages of 311 ± 5.8 Myr (MSWD = 0.21) and 307 ± 14.6 Myr (MSWD = 0.22), within errors, using the ^{207}Pb-based common-lead correction[59]. Similarly, a lower intercept age of 315 ± 8.2 Myr (with upper intercept at $^{207}Pb/^{206}Pb = 0.97 ± 0.06$, MSWD = 1.4, $n = 23$) and a weighted mean $^{206}Pb/^{238}U$ age of 303 ± 9.0 Myr (MSWD = 0.83) were obtained for LT eclogite (AT47, Supplementary Fig. 7c). Eleven and twelve spots of zircon grains, respectively, from HT and LT eclogites (AT54 and 47) were measured for trace element compositions and U-Pb dating (Supplementary Data 7–8). The Th/U ratio of all zircons vary from 0.64 to 2.43, mostly >0.85. Blurred core-rim structure was observed for a few grains but most of rims were too narrow to be analyzed (<10 µm). Core domains of zircons from HT and LT eclogites (Supplementary Fig. 7d, e) give concordia ages of 350 ± 5.1 Myr (MSWD = 6.2, $n = 11$) and 398 ± 4.1 Myr (MSWD = 3.6, $n = 12$), respectively, in accordance with their weighted mean ages of 349 ± 6.9 Myr (MSWD = 7.9) and 394 ± 4.4 Myr (MSWD = 2.2). To be stressed, REEs patterns of analyzed zircons (Supplementary Fig. 7f) uniformly show positive slope from LREEs to HREEs with obvious Eu negative abnormal, typical of zircon with igneous origin[60].

Compilation of age and geochemical data of regional rocks. To elucidate the nearly simultaneous crustal and mantle responses in upper plate (i.e., KYCTC) during which the thermal excursion occurred and witnessed by the formation of HT eclogites within the subduction plate interface, we fingerprint the spatial and temporal variation and evolution of regional magmatism, deformation and metamorphism, based on systematic geochemical and chronological data collection of various lithologies (Relevant references are listed in Supplementary Data 10–13) among the STOB. This includes: (1) 403 arc intermediate rocks (including adakite, Figs. 5, 6b, e, Supplementary Fig. 11, Supplementary Data 10) and 753 granites (Fig. 6d, Supplementary Fig. 12, Supplementary Data 11) with complete major and trace element compositions, radiometric ages, and bulk-rock Sr-Nd isotopic data; (2) 74 metamorphic rocks with radiometric ages and P-T estimate from the Atbashi and Akeyazi LT-(U)HP metamorphic complexes in the STOB (Fig. 6a, Supplementary Data 12); (3) A compilation (Fig. 6c, d, Supplementary Data 13) of 142 age data of regional metamorphism, fossils in depositing basin, and main strike-slip faulting & thrusting events was also conducted for chronological comparison. Bulk-rock Hf/Nd, Nd/Sr, Sr/Y, $^{87}Sr/^{86}Sr$, and $^{143}Nd/^{144}Nd$ elemental ratios were then utilized as proxies (Figs. 5, 6) to differentiate metamorphic and magmatic products with distinct source signatures and their spatial-temporal evolution, along with crust-mantle responses, during the continuous subduction of the STO. The compilation of zircon Lu-Hf isotopic data, together with ages, from igneous and sedimentary rocks[37] and the regional ophiolite ages[46,61,62] are presented for comparison. Compositions of relevant geochemical endmember mixing components are present in Supplementary Data 14.

Discussion

Eclogitic mélange rocks and thermal excursion. Direct geophysical investigation, although facilitating observations of subarc processes, does not provide the resolution required to obtain detailed micro-scale information of material transfer at the slab-mantle interface[19]. In contrast, the chemical and isotopic composition of metamorphic products and arc lavas serve as the best candidate to extract information on this critical realm of the subduction zone. Completely distinct geochemical features characterize studied eclogites in the Kembel mélange of the ATMC. Of these, HT eclogites are of intermediate composition (SiO_2 ~52 wt %) with moderately varying values of TiO_2, FeO_{tot}, MgO, and CaO (Supplementary Data 3), and exhibit moderate enrichments in LILEs (e.g., Rb, Ba, Sr), HFSEs (e.g., Th, Nb, Ta) and LREEs, with relatively higher $^{143}Nd/^{144}Nd$ but lower $^{87}Sr/^{86}Sr$ isotopic ratios, compared to those of relatively mafic LT ones (Fig. 5, Supplementary Fig. 6b, d, e). In addition, HT eclogites present slightly Nb-Ta negative abnormal with ambiguous similarity to those of subduction-related lavas[63,64], average mélange rocks[5] and corresponding compositions of their modeled[65] and experimental[9] melts in trace element pattern (Supplementary Fig. 6d). Whereas close resemblance to those of depleted mantle[66] (DM) and altered oceanic crust[67] (AOC), without any Nb-Ta negative abnormal, is tied to LT eclogites. Further evidence comes from their sharp discrimination in Th/Yb-Nb/Yb diagram (Supplementary Fig. 6b) and εNd(t) values (~2.2–4.9 versus ~2.6–8.6; Supplementary Data 4), calling for in-depth inquiry to the petrogenesis and protolith as echoed by the fractionation of key trace elements and isotopes during which normal melting processes (e.g., at mid-ocean ridges[68]) and/or material transport from descent slab to overlaying metasomatized mantle[63,64,69] took place. In Sr-Nd isotopes, Nd/Sr and Hf/Nd diagrams (Fig. 5), LT eclogites predominantly gather around the domain of DM and AOC with broadly unperturbed trace element and radiogenic isotope ratios, implying an origin of slab mafic components. By
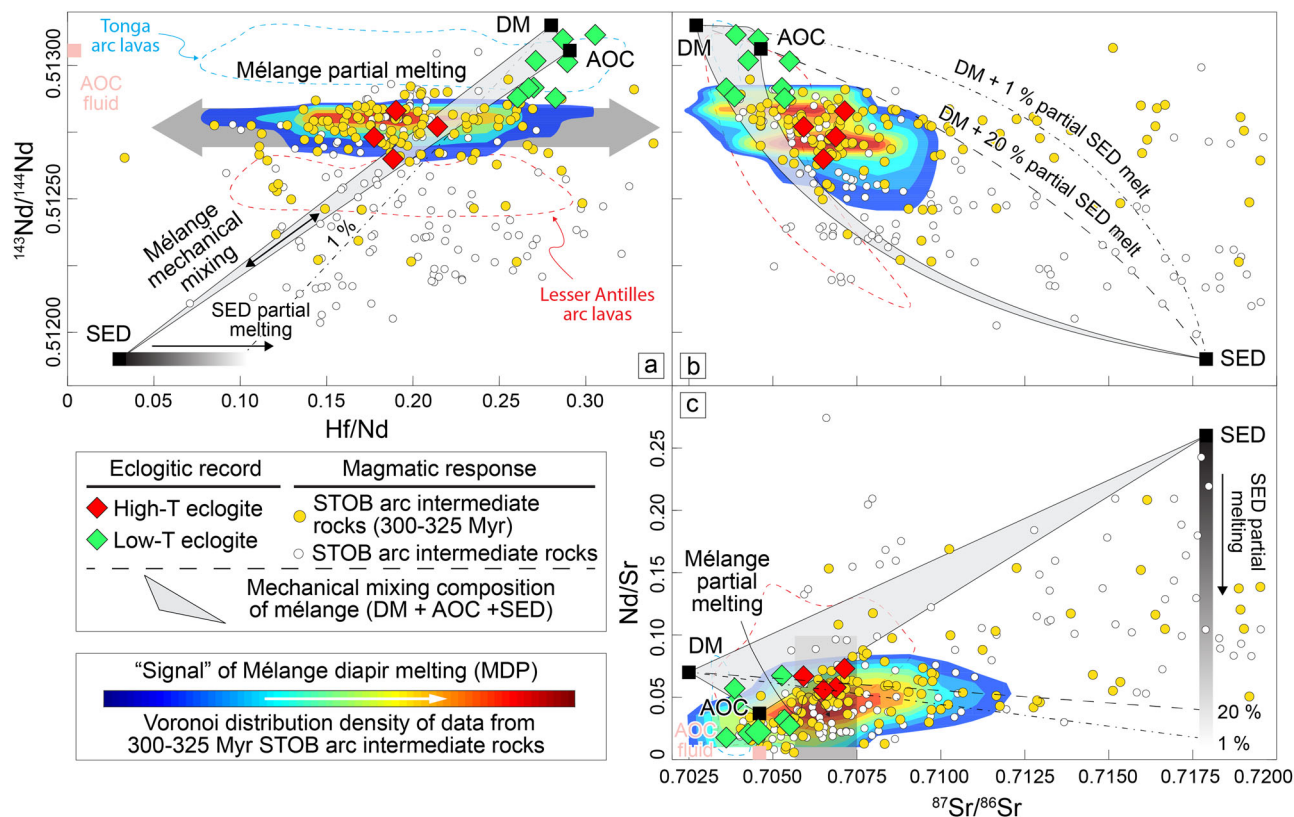
Fig. 5 Plot of Sr-Nd isotopes versus key trace elements ratios. a, b, c ^{143}Nd/^{144}Nd, ^{87}Sr/^{86}Sr against Hf/Nd, Nd/Sr ratio plots; gray arrows paralleled to axes of Hf/Nd and Nd/Sr ratios indicate substantial fractionation caused by mélange melting with limited variations in ^{143}Nd/^{144}Nd and ^{87}Sr/^{86}Sr; literature data are collected from the GEOROC database (http://georoc.mpch-mainz.gwdg.de/georoc/); the compilation of STOB arc intermediate rocks is present in Supplementary Data 10; mixing lines between the mantle and bulk sediment and between the mantle and sediment melts are shown as examples; the black-gray bar illustrates the range of sediment melts possible for sediment melting down to a degree of as little as 1%; sediment melts were computed by using relative partition coefficients of D_{Sr} = 7.3, D_{Nd} = 0.35 and D_{Nd}/D_{Hf} = 0.9–4.3 in accordance with the data observed in experiments by ref. [16] over the temperature range of 750 to 900 °C; sources and compositions of endmember mixing components are list in Supplementary Data 14.

comparison, noteworthy deviation, aloof from DM and AOC endmembers, is bound to HT eclogites, suggesting a protolith of hybrid chemical composition with the addition of substantial sedimentary component. Since AOC-derived fluids generally have too low Hf/Nd and Nd/Sr ratios and distinctly higher ^{87}Sr/^{86}Sr[19,67], this eliminates fluid from slab as the major end-member responsible for generating the Sr-Nd elemental & isotopic ternary mixing space overlapped with studied HT eclogites. Experimental works[7,15,16] demonstrate that a combination of partial melting of subducted sediments and AOC metamorphic dehydration could be of capability to produce required trace element fractionations as observed in global arc lavas[19,69,70] and HT eclogites in this study (Fig. 5, Supplementary Fig. 6). Yet, fairly high ^{87}Sr isotopic composition and sharp Sr-Nd isotopic curvature, as well as extremely low Nd/Sr ratio, of simple sediment melts[71] would yield ternary mixing domain far deviated from data of studied HT eclogites. In short, it follows that the Sr-Nd isotope systematics of HT eclogites evaluated here (Fig. 5b, c) denote a potential physical mixing[26,72] of DM and AOC with ~2–4 weight percent of bulk sediments, which leads to the formation of hybrid rock types, rather than the direct addition of melts and/or fluids from slab components (e.g., sediment, AOC). Noteworthy, the relatively minor sediment component in some natural mélange, which is also mirrored by the amounts of sediment contribution in global arc lavas (Fig. 5), does not preclude the formation of accessory minerals and corresponding trace elements fractionation if mélange contains substantial AOC component[9,19].

The finding of key index minerals (i.e., the existence of Mg-rich garnet, Fe-rich clinopyroxene, ilmenite, and high Zr content rutile, Fig. 3a–c, Supplementary Figs. 1, 4) and contrasting petrological features (i.e., the preservation of massive irregular patches of quartz and pseudomorphs after melt films, Fig. 3a, b, Supplementary Figs. 1a–c, 2g, h) as well as P-T constraints retrieved from multi-methodology approaches (Fig. 4a, Supplementary Figs. 4c, 8, 9), collectively suggest a contrasting thermal history of studied eclogitic mélange rocks with substantial heating, after peak burial, to HT condition (~810 °C, Fig. 4a, Supplementary Fig. 8). Alternatively, oversteeping breakdown of epidote group mineral via a reaction like cpx + zo = grt + qz + H_2O may generate observed patchy quartz textures in garnets of HT eclogites. However, their relatively poor concentration of bulk-rock CaO (~7.8 wt%, compared with ~12.3 wt% of that of LT one; Supplementary Data 3) could essentially rule out this possibility, especially to condition >700 °C (Supplementary Figs. 8, 9; ref. [73]). To be stressed, numerous previous estimates (in average of 2.8 GPa and 540 °C, as reviewed by refs. [33,74]; Fig. 4) and plenty of lawsonite[39,75–77] and coesite[32,35,38,78] reports, as well as the presence of closely associated LT eclogites in the region (Figs. 1, 2), had confirmed the STMC is of close resemblance to a deep preserved subduction plate interface[32,79], plausibly standing in contradiction with such an extraordinary eclogite-facies thermal excursion (ΔT ~250 °C, Fig. 4a). Several processes can be envisioned for "unusual" heating: (1) Fluid, released from descant slab, could drive exothermic carbonation and hydration reactions in the subduction plate interface or
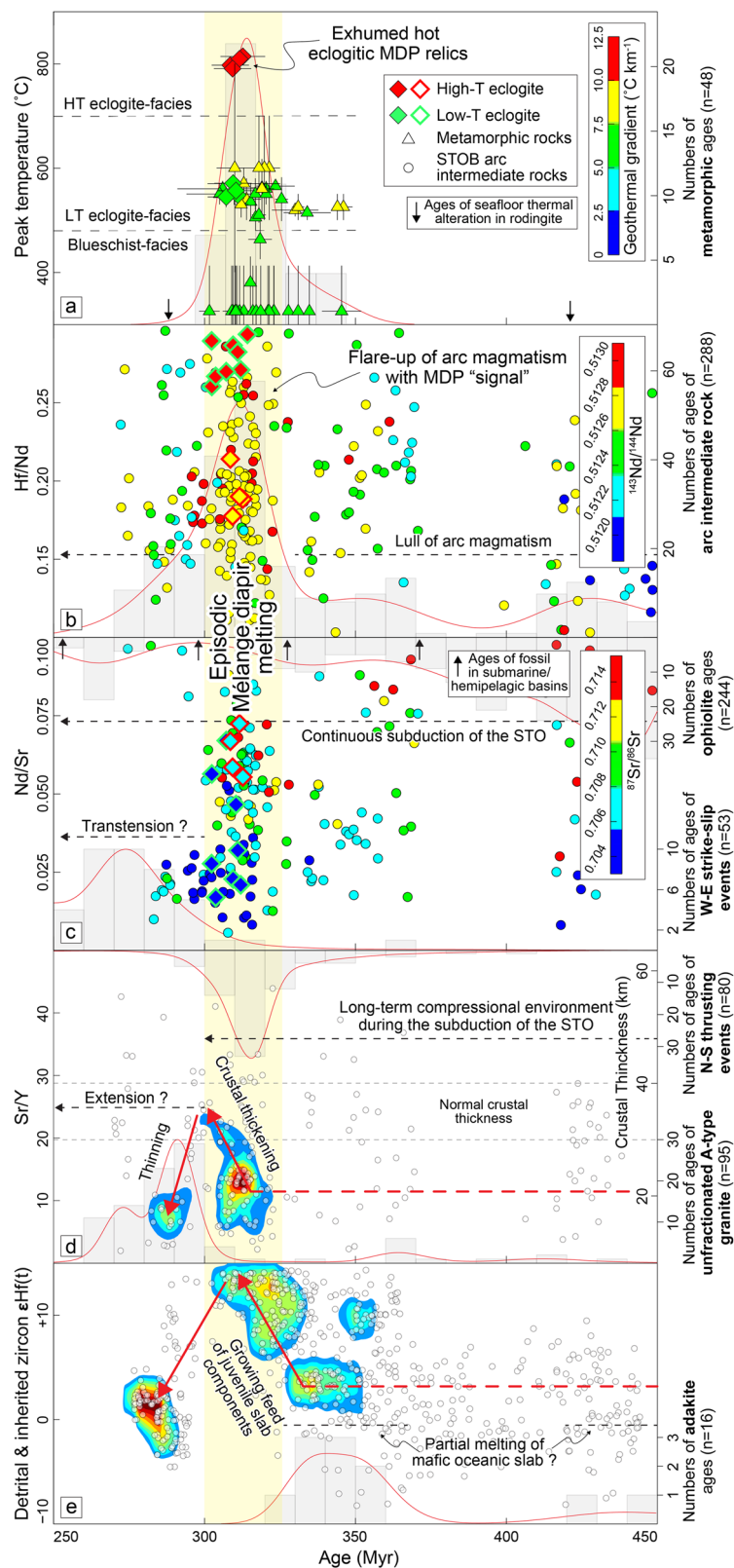
Fig. 6 Plots of compiled multi-disciplinary evidence. a The temporal evolution of the peak temperature of metamorphic rocks in the STMC; geothermal gradient is shown as color bar; ages of seafloor thermal alteration in rodingite, as marked by black arrows, are from ref. [153]. **b, c** Ages against the Hf/Nd and Nd/Sr ratios of arc intermediate rocks in the STMC; $^{143}Nd/^{144}Nd$ and $^{87}Sr/^{86}Sr$ are highlighted as color bar; ages, marked by black arrows, of fossil in submarine/hemipelagic basins are from refs. [54,154]. The temporal evolution of **d** the Sr/Y ratio of arc intermediate rocks and **e** detrital & inherited zircon εHf(t) of (meta-)sedimentary & igneous rocks in the STMC; data distribution of scatter plot is evaluated by Voronoi density[155]. Histograms are also plotted from compiled regional data, listed in Supplementary Data 10–13, for comparison.

overlying mantle wedge[80] with temperature increasing up to 75–200 °C at high convergent rate ~10 cm yr⁻¹ and P ~1.0 GPa[81]. However, pervasive hydration seems impossible at such depths in UHP eclogite-facies condition[33]; (2) Heat advection from syn-metamorphic mafic magmas together with potential fluid flow and/or radioactive decay could contribute to the thermal "budget", but is likely to be <30 °C along the subduction plate interface[80,82]; (3) Shear heating, which is proportional to velocity times rock strength, could in principle modify the thermal budget along the subduction thrust by up to ~200 °C[80,83], but would be limited in fluid-rich environments or buffered by endothermic dehydration reactions (i.e., lawsonite and chlorite) predicted across the refrigerated temperature range of the STMC. Besides, none of eclogitic mylonites and/or ultra-mylonites, advocating for high strain, are observed in region[33,51,74]; (4) Convective motion of subducted materials could also strongly affect heat transport and temperatures[80,84,85]. It is effectively limited to depths greater than 80 km, as the "cold nose" with low-seismic attenuation is frequently observed[86,87] and expected[88,89] to be a comparatively rigid part of the upper mantle wedge, indicating relative isolation from heat flow[88]. Although deeply tectonic slicing and stacking of UHP metamorphic volcanoclastic sequence were locally envisioned in the Akeyazi area[32,33,74], the LT-(U)HP metamorphic complexes (i.e., the Atbashi[51], Chatkal[48,49] and Fan-Karategin[50] sections) across the entire STMC are mainly dominated by the exposure of blueschist-/eclogite-facies mafic blocks wrapped by meta-sedimentary host rocks (500–600 °C, 2.0–3.0 GPa). They constitute the architecture of deeply subducted and cooled sedimentary mélange with relatively low bulk viscosity[32,84,85] (compared to rigid overlaying and descending plates), which could facilitate the efficient fluid circulation[90] and ensure convective motion[91] within subduction plate interface and/or short-lived translation[34] toward the hot corner of mantle wedge. Thus, substantial thermal excursion after peak burial, which was exactly across the wet solidus of basic to intermediate composition (Supplementary Fig. 8), as witnessed by studied HT eclogitic mélange rocks could, in fact, disclose the potential translation of mechanical mixed subducted materials nearer to a relatively hotter mantle wedge and meanwhile farther away from the refrigerated subduction plate interface.

Mélange diapir melting in refrigerated subduction plate interface. Plentiful studies[69,92] tie the chemistry of the arc magma to a variable contribution from the DM, AOC, and slab sediments. However, experimental petrology studies have faced challenges in simultaneously reproducing both major and trace element features of the most common types of arc magmas[20]. Nevertheless, recent debates challenge the traditional model, which attributes characteristic trace element signal of arc magmas solely to hybridized mantle wedges formed through discrete feedings of fluids and/or aqueous melts from slab components[9,19]. Alternatively, trace element and isotope variability in global arc magmas can be adequately explained only if physical mixing of DM, AOC, and sediments occurs early within the plate interface during subduction, before melting begins[5]. This revised pre-requisite essentially substantiates the momentous role of mélange in arc magmatism. Although kilometers-thick low-seismic velo-city regions atop subducting slabs worldwide could imply the existence of mélange zones at the slab-mantle interface[26–28], direct field evidence confirming extensive exhumation of buried sediments along the plate interface remains scarce, further hampering a comprehensive assessment of the extent of chemical and/or mechanical disruption of subducted materials within the plate interface. To be stressed, massive sediment accretion at ~80 km depth along the subduction interface has been recently

disclosed in the STMC[32,33], denoting continuous refrigeration, by incoming cold material from the slab, and juxtaposition to the "cold nose" of mantle wedge. In addition, short-lived thermal pulse (~80 °C, to 600 °C within ~300 Kyr) was revealed from unusual garnet zonation in coesite-bearing oceanic eclogites[34], advocating potential translation of UHP refrigerated slices to a relatively hotter mantle wedge. In particular, the trace element and Sr-Nd isotope systematics of HT eclogites evaluated here (Fig. 5b, c) denote a probable physical mixing[26,72] of DM and AOC with bulk sediment, leading to the formation of mélange rocks, instead of the addition of melts and/or fluids from slab components. The discovery of massive irregular patches of quartz, which resembles granitoid products from melt experiments for pelitic to felsic lithologies[6], and "nano-diorite" pseudomorphs after melt films in studied HT eclogites (Fig. 3a, b, Supplementary Figs. 1a–c, 2g, h) as well as P-T constraints retrieved from multi-methodology approaches (Fig. 4a, Supplementary Figs. 4c, 8, 9), jointly suggest a striking thermal history of studied eclogitic mélange rocks with substantial heating, after peak burial, to the condition rightly crossing the wet solidus on pseudosection of basic to intermediate composition (~810 °C, Fig. 4a, Supplementary Fig. 8). Such translation toward the hot corner of mantle wedge could be short-lived around several hundred thousand to several million years if considering the limited gap between the ~312 ± 2.7 Myr cooling timing of HT eclogitic mélange rocks and the ~315 ± 8.2 Myr crystallization age of LT oceanic eclogites (Fig. 4a, Supplementary Figs. 4c, 7a–c). It also broadly meets the timeframe of 0.01–1.0 Myr[21,25], with a range of modeling parameters, for the mantle wedge diapirs rising from the slab to the magma chamber. This short-lived ~250 °C thermal excursion lasting ~1.65 Myr in average would correspond to displacements on the order of ~0.2 to 2 cm yr⁻¹ assuming a thickness[32,79] between 0.5 and 5 km for the subduction plate interface (in the broad range of geophysical imaging[93], i.e., 2–5 km), compatible, in any case, within the range of typical exhumation rates worldwide, either for (U) HP oceanic or continental rocks (~1-5 mm yr⁻¹, or ≥ cm yr⁻¹, respectively)[30]. Yet, extremely high exhumation velocity, to ~40–45 cm yr⁻¹, of diapiric stokes flow, between depths of 50 to 80 km within the subduction plate interface, was locally reported from the Akeyazi UHP metamorphic complex in the China segment of the STOB[94].

It is noteworthy that almost all (>95%) Late Carboniferous arc intermediate rocks, which constitutes a flare-up period of Late Paleozoic magma emplacement in the STOB (i.e., the Central Tianshan Arc[95]), uniformly show signal of MDP with horizontal Hf/Nd arrays but little variation in $^{143}Nd/^{144}Nd$ (Figs. 5, 6b, c), serving as potential magmatic products in lower crust echoing with the simultaneous direct HT eclogitic records (Figs. 3a–c, 4a) near subarc depth supporting mélange diapir took place and subsequent trace element fractionation (main Hf/Nd, Nd/Sr) caused by mélange partially melting[19]. Such a Late Carboniferous flare-up of arc magmatism with MDP signal is coupled with noteworthy crustal thickening associated with production of high magma volumes[96] (~40 km³ (km Myr⁻¹)⁻¹) along with relatively long-term compressional environment[33,97] during the subduction of the STO (Fig. 6d). Thick crust, which will suppress mantle wedge melting and enhance intra-crustal differentiation[65,98], could also offer a favorable condition for the generation of intermediate melts (e.g., sedimentary mélange melting during diapirism[6]). In addition, growing feed of juvenile slab components (Fig. 6e) almost contemporaneously follows with this period, suggesting a potential tectonic scenario with melted equivalents of mélange rocks buoyantly rise toward hot mantle wedge, generate magmas with MDP signal and occasionally leave partially melted HT eclogitic relics exhumed physically to shallow depths along the refrigerated subduction plate interface after
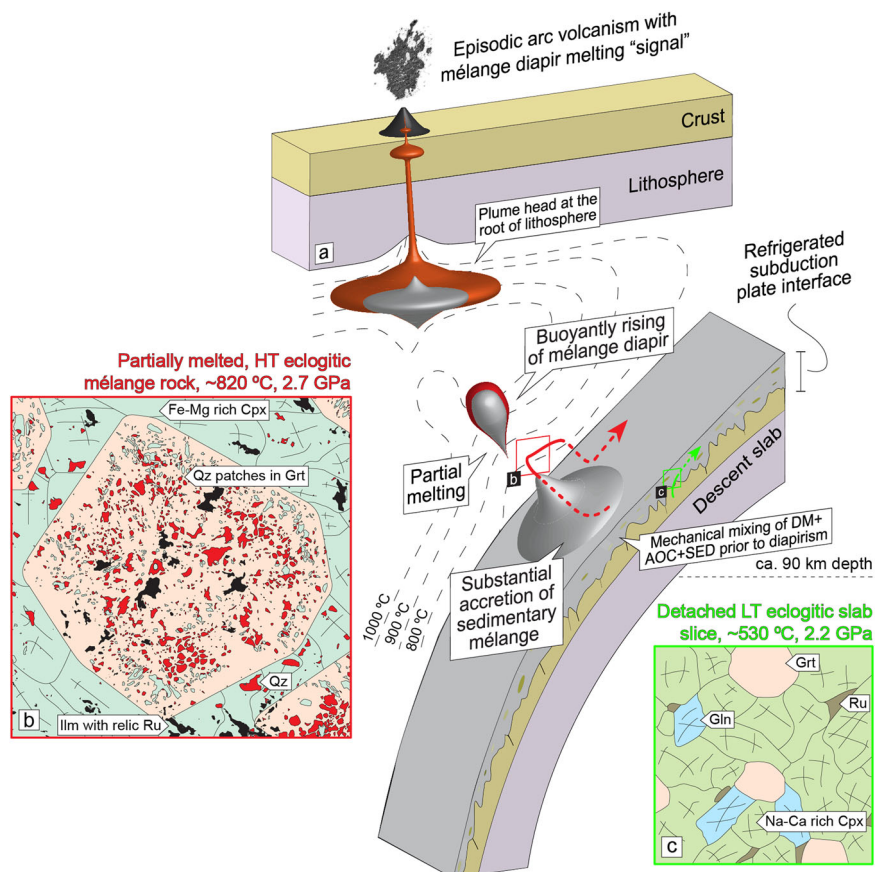
Fig. 7 3D schematic drawing of the first tangible rock records substantiating mélange diapir melting model. Deeply accreted mélange and its buoyantly raised diapir are marked in gray with melt zones highlighted in red. Red arrow indicate trajecty of studied HT eclogites entrained in a mélange diapir within refrigerated subduction plate interface, and green path of LT eclogite is also show for comparison with insets depict their contrasting petrological and petrographic features.

thermal excursion (Fig. 4a, 7), with subsequent latent oceanic slab roll-back and break-off.

Implications for volatile recycling. The devolatilization of subducting slabs serves as a critical role in the melting of mantle wedge, generation of arc magmas, and regulation of global geochemical cycles. Petrological Modeling[12,99,100], based on geophysical observation of thermal structure of global subduction zones, discloses that volatile (up to ~33–66% mineralogically bound H_2O and ~65–95% CO_2 in slab lithospheric components) could efficiently pass through old and fast, namely cold, subduction zones (e.g., Honshu in the western Pacific). Whereas much weighty proportion of volatile derived from the slab could be lost beneath the forearc in hot subduction zones (e.g., Cascadia). On average, as representative of the range of thermal conditions in modern arcs[89], about four fifths of CO_2 and one third of H_2O are retained within slab beyond the subarc[12,99], regulating the Earth with secular cooling[13,101] as the efficiency of volatile recycling, to deep mantle (e.g., ≥240 km[99]), increased over the Proterozoic and Phanerozoic. The principal volatile components in subducting lithologies are respectively bound in carbonated and hydroxylated minerals within marine sediments, hydrothermally AOC, and serpentinized upper oceanic mantle[12,102]. Though controversy exists regarding the melting of subducted lithologies as a potential source for arc volcanism and the mobilization of volatile, nearly all melting in subduction settings requires the presence of fluid[70,103]. Yet the mechanism of fluid flow propagation (i.e., pervasive *versus* channelized[10–12]) and the

fact of Phanerozoic secular cooling of Earth mantle[13], indeed, hinder the efficiency of volatile mobilization beneath the subarc, further making the feeding of subducted volatile into the mantle wedge remains ambiguous[14].

Alternatively, considerable amounts of volatile (H_2O ~1.0–11.8, CO_2 ~1.2–9.7 wt%; see ref. [5] for systematic review) are enriched in mélange rocks, comparable to those in oceanic slab components[14,102,104]. It could potentially act as a temporary carrier of H_2O, CO_2, and sulfur with relatively low bulk viscosity and density[25] facilitating the hybridization of mantle wedge and the transformation of volatile from descent slab to arc magmas. Such process, as widely refers as buoyant diapirism[5,20] of high-pressure mélange, invokes physical mixing of slab components and mantle wedge and generates arc magmatic products, with MDP signal[19] (e.g., Figs. 5, 6) which were identified globally from representative arcs (e.g., Tonga[19], Aleutians[70] and Marianas[69]). In addition, mélange melting at the top of the slab could potentially record residual garnet fingerprint[19], such as high Sr/Y and HREEs depletions as observed in many arc lavas, although it have been classically interpreted to reflect melting of the subducted basaltic crust at high pressure[105]. Experimental[20,23,106] and field-based studies[107–110] point to the presence of orthopyroxenites may also potentially record the hybridization of mantle wedge by mélange materials. Besides, the abundance of [10]Be and the common existence of positive Sr anomalies in arc lavas indicate non-negligible contribution from subducted ocean-floor materials (sedimentary and oceanic crustal sources) to arc magmas[111,112]. Locally, channelized HP veins[113,114], carbonated eclogites[115] and graphite-rich eclogitic meta-sediments and meta-basalts[116,117]

were well preserved in the STMC, making a valuable nature "laboratory" of volatile-rich deeply buried mélange "package". The fact that carbonates in eclogitic meta-basalts show mantle-like C-O isotopic features while marbles have sedimentary carbonate isotopes[115,116] essentially disclose the necessity of a momentous contribution of carbonate-rich oceanic slab components in generating alkaline arc lavas[65]. CO_2-bearing reactive fluid flows were emphasized[118] only at the slab-wedge interface without being emitted to the volcanic arc or transported deeper into the mantle, further implying a great capacity of mélange diapir scenario in recycling volatile. In particular, the trace element and Sr-Nd isotope systematics of HT eclogites evaluated here (Fig. 5b, c) denote a probable physical mixing[26,72] of DM and AOC with bulk sediment, leading to the formation of mélange rocks, instead of the addition of melts and/or fluids from slab components. The discovery of key mineralogical evidence (Fig. 3a, b, Supplementary Figs. 1a–c, 2g, h), together with P-T constraints (Fig. 4a, Supplementary Figs. S4c, 8, 9), jointly suggest a striking thermal history of the mélange "package" (as witnessed by studied eclogitic mélange rocks) with substantial heating, after peak burial, to the condition rightly crossing the wet solidus of basic to intermediate composition (~810 °C, Fig. 4a, Supplementary Fig. 8). Such translation, which could be short-lived around several hundred thousand to several million years, toward the hot corner of mantle wedge could serve as the first tangible rock records (Fig. 7) supporting mélange diapirs may, indeed, propagate, and dynamically mix with the overlying mantle as conceptual vitalization[5,19,20] and modeling[23,25] predicted. Coincidently, the contemporaneous Late Carboniferous flare-up of regional arc magmatism with MDP signal, which is coupled with production of huge magma volumes[96], collectively suggests a viable and non-negligible process of the hybridization of mantle wedge by buoyant mélange materials, to transfer volatile, generate arc lavas and regulate terrestrial geochemical cycles, stands.

Methods

Microprobe analysis. The major element compositions of pivotal minerals in the eclogites investigated were determined through electron microprobe analyses of polished thin sections. These analyses were conducted at Wuhan Sample Solution Analytical Technology Co., Ltd., China, utilizing a Jeol JXA-8100 instrument. Quantitative measurements were performed with wavelength dispersive spectrometers, featuring an acceleration voltage of 15 kV, a beam current of 15 nA, a 3 μm beam size, and a counting time of 30 s. Reference standards, both natural minerals and synthetic oxides, were employed, and data correction was carried out using a program based on the ZAF procedure. Detailed information regarding the samples, their mineral assemblages, and the results of representative microprobe analyses of key minerals are presented in Supplementary Data 1 and 3, respectively.

Bulk-rock major and trace elements analysis. The analysis of major element compositions was carried out at the Institute of Geology and Geophysics, Chinese Academy of Sciences. Major oxide concentrations were determined using a Phillips PW1480 X-ray fluorescence spectrometer (XRF) on fused glass disks. Loss on ignition (LOI) was measured following heating to 1000 °C. Most major oxides had uncertainties of approximately 2%, while MnO and P_2O_5 displayed deviations of around 5%. The total measurements consistently fell within the range of 100 ± 1 wt%. Whole rock Fe_2O_3 content was determined via potassium permanganate titration[119]. Trace element concentrations were assessed through sector field inductively coupled plasma mass spectrometry (ICP-MS) using a Finnigan MAT ELEMENT

spectrometer at the Institute of Geology and Geophysics, Chinese Academy of Sciences. Relative standard deviations (RSD) were generally within ± 10% for most trace elements, though they extended to ± 20% for V, Cr, Co, Ni, Th, and U, based on rock standard analyses. Detailed major and trace element analyses, as well as the comprehensive bulk-rock major element composition for thermodynamic modeling, are presented in Supplementary Data 2.

Bulk-rock Sr-Nd isotope analysis. High-precision isotopic measurements for the eclogites under investigation, specifically Sr and Nd isotopes, were performed at Nanjing FocuMS Technology Company. The methodology involved the mixing of geological rock powders with 0.5 ml of 60 wt % HNO_3 and 1.0 ml of 40 wt % HF in high-pressure PTFE bombs. These steel-jacketed bombs, designed for safety, were subjected to 195 °C in an oven for a duration of 3 days. Following this, the digested samples were desiccated on an HTplate and reconstituted in 1.5 ml of 1.5 N HCl before undergoing ion exchange purification. The elutions containing Sr and Nd were gently evaporated to dryness and subsequently re-dissolved in 1.0 ml of 2 wt % HNO_3. To further enhance precision, a diluted solution (0.05 μg g^{-1} Sr, 0.05 μg g-1 Nd) was introduced into the Nu Instruments Nu Plasma II Multi-Collector ICP-MS (MC-ICP-MS) in Wrexham, Wales, UK, through the Teledyne Cetac Technologies Aridus II desolvating nebulizer system in Omaha, Nebraska, USA. Raw data for isotopic ratios were internally corrected for mass fractionation by normalizing to specific ratios, namely $^{86}Sr/^{88}Sr = 0.1194$ for Sr and $^{146}Nd/^{144}Nd = 0.7219$ for Nd, using the exponential law. International isotopic standards, such as NIST SRM 987 for Sr and JNdi-1 for Nd, were periodically analyzed to rectify instrumental drift. Quality control measures were upheld through the analysis of geochemical reference materials, namely USGS BCR-2, BHVO-2, AVG-2, and RGM-2. The isotopic results obtained during this study were in agreement with those reported in prior publications, and the analytical uncertainties were well within acceptable limits[120]. Detailed Sr-Nd isotopic data of studied samples and modeling parameters are given in Supplementary Data 4.

Laser ICP-MS trace element analysis of rutile and quartz. Quantitative trace element analysis of rutile and quartz was performed in situ using separate laser ablation systems. For rutile analysis, the ESI New Wave NWR 193UC (TwoVol2) laser ablation system was employed, connected to an Agilent 8900 ICP-QQQ at Beijing Quick-Thermo Science & Technology Co., Ltd. Simultaneously, the analysis of quartz was carried out using a double focusing sector field ICP-MS instrument, specifically the Finnigan MAT model-ELEMENT, at Wuhan Sample Solution Company. These analyses were conducted on polished 50 μm-thick thin sections and selected mineral grains embedded in epoxy resin from the studied eclogites. Helium served as the carrier gas to enhance the transport efficiency of the ablated material, which was mixed with makeup gas (Ar) prior to entering the ICP, ensuring the maintenance of stable and optimal excitation conditions.

In the case of rutile analysis, a 193 nm (ArF excimer) argon fluoride New Wave Research Excimer laser ablation was conducted, lasting for 30 s. This process featured a 40 μm diameter beam size, delivering an energy of approximately ~4 J cm^{-2} and operating at a repetition rate of 5 Hz. Rutile analysis was carried out on the selected grains and reference materials after an initial 10-s baseline signal collection and 3 pulses of pre-ablation. Calibration of trace elements was achieved using NIST SRM 610 glass, with the internal standard major

element Ti. These reference materials were analyzed twice, both before and after each analytical session, covering 6–8 spots on mineral samples. The data underwent background subtraction and correction for laser-induced elemental fractionation down-hole, a process facilitated by the Iolite data reduction package integrated within the Wavemetrics Igor Pro data analysis software[121].

For quartz, laser ablation was conducted using a Finnigan MAT UV laser probe operating at 266 nm. The laser was operated with a pulse width of 3 ns (Q-switched), a sHT frequency of 20 sHTs s[-1], a pulse energy of 0.5 mJ, and a spot size of 30 μm on rasters not exceeding 300×300 μm. To optimize the operating parameters of the ICP-MS, ablation of the reference material NIST 612 was carried out using ^{139}La, with a focus on achieving maximum sensitivity and stability. Si contents, determined from the chemical formula, served as the internal standard for evaluating element abundance.

The acquisition time was structured with 20 s allotted for background measurements and 120 s for mineral analyses. External calibration standards were established using glass reference materials NIST SRM 610 and NIST SRM 612. The reproducibility and accuracy, as determined with NIST SRM 610 and NIST SRM 612, typically yielded results of less than 8% and 6%, respectively. Trace element concentrations were subsequently calculated using GLITTER Version 3[122]. Summary of apparent concentration of Zr and Ti of rutile and quartz, respectively, from different domains (i.e., in matrix and as inclusion in garnet) in studied eclogites were giving in Supplementary Data 5 and 6.

Laser ICP-MS U-Pb isotope analysis of zircon. Zircons were separated from samples processed by crushing, heavy-liquid, and magnetic methods and then were mounted in epoxy resin and polished to expose the interior. Subsequent to this preparation, cathodoluminescence (CL) imaging of the zircons was carried out using a scanning electron microscope at the Institute of Geology and Geophysics, Chinese Academy of Sciences. This step was integral in the selection of suitable zircon grains and the identification of optimal target sites for U-Pb dating. The U-Pb dating and the concurrent analysis of trace element composition in both rutiles and zircons were conducted using LA-ICP-MS at Wuhan Sample Solution Analytical Technology Co., Ltd., China. The operating conditions for the laser ablation system, the ICP-MS instrument, and the data reduction procedures were consistent with those described in ref. [123]. Laser sampling was executed with a GeolasPro laser ablation system, comprising a COMPexPro 102 ArF excimer laser (with a 193 nm wavelength and a maximum energy of 200 mJ) and a MicroLas optical system. Ion-signal intensities were measured using an Agilent 7700e quadrupole ICP-MS instrument, with helium employed as the carrier gas. To maintain stability, argon was introduced as the makeup gas and mixed with the carrier gas via a T-connector before entering the ICP. Significantly, the laser ablation system was equipped with a "wave" signal smoothing device[124]. the laser's spot size was set at 60 μm, and the frequency was maintained at 6 Hz. External standards, specifically zircon 91500 and glass NIST610, were used for U-Pb dating and trace element calibration, respectively. Each analysis began with a background acquisition period of approximately 20–30 s, followed by 50 s of data acquisition from the sample. To ensure accuracy, an Excel-based software, ICPMSDataCal, was employed for off-line selection and integration of background and analyzed signals, time-drift correction, and quantitative calibration for trace element analysis and U-Pb dating[125]. Concordia diagrams and weighted mean calculations were made using Isoplot/Ex_ver3[126]. Relevant data is listed in Supplementary Data 7 and 8.

SIMS U-Pb isotope analysis of rutile. U-Pb isotope measurements were conducted using the Cameca IMS 1280 ion microprobe at the Institute of Geology and Geophysics, Chinese Academy of Sciences. utile crystals were meticulously prepared by embedding them in transparent epoxy alongside reference standards. These reference standards included the R10 rutile standard (~30 μg g^{-1} U, Concordia age = 1090 ± 5 Myr)[127], 99JHQ-1 rutile (highly variable U content with average of 2 μg g^{-1}, ^{206}Pb/^{238}U age = 218 ± 1.2 Myr)[128], and an in-house rutile megacrystal standard (JDX) (~6 μg g^{-1} U, ^{207}Pb/^{206}Pb age = 521 Myr, ^{206}Pb/^{238}U age = 500–520 Myr, unpublished TIMS data). The samples were carefully polished to expose the pristine interior of the crystals. Subsequently, the mount was coated with high-purity gold prior to ion probe analysis. The primary ion beam employed was O$_2$, accelerated to 13 kV with an intensity of approximately 15 nA. The aperture illumination mode (Kohler illumination) was utilized, featuring a 200 μm aperture to ensure uniform sputtering across the entire area of analysis. The spot size was approximately 20×30 μm, displaying an ellipsoidal shape. Positive secondary ions were extracted using a 10 kV potential. The mass resolution of ~6000 was used and the magnet was cyclically peak-stepped through a sequence including the ^{206}Pb$^+$, ^{207}Pb$^+$, ^{208}Pb$^+$, U$^+$, UO$^+$, ThO$^+$, UO$_2^+$ and ^{49}TiO$_4^+$ to produce one set of data. A single ion-counting electron multiplier (EM) was used as the detection device. The ^{49}TiO$_4^+$ signal was selected as a reference peak for aligning the secondary ion beams due to its robust intensity and lack of interference from ZrO. Each measurement cycle consisted of 10 cycles, and the total analytical time was approximately 15 min, inclusive of 2 min of rastering before the actual analysis to reduce the impact of surface-contaminant Pb. It's worth noting that the consideration of mass fractionations of Pb isotopes and Pb hydrides, which would necessitate a mass resolution exceeding 30000, was omitted. Several studies have corroborated the negligible impact of these effects and their mutual cancellation[129]. Relevant data is listed in Supplementary Data 9.

Zr-in-rutile thermometer and Ti-in-quartz thermobarometer. Three commonly applied calibrations[56,57,130,131] were used to estimate temperatures in dependent of Zr concentrations in rutile. We considered a pressure value of 2.7 GPa (for the calibration of ref. [57]) in accordance with P-T estimates via thermodynamic modeling (Supplementary Figs. 8, 9) for both HT and LT eclogites, and with the finds of coesite in adjacent area (i.e., the Akeyazi metamorphic complex in the STOB, as reviewed by ref. [33]). The activity of ZrSiO$_4$ was set to unity because minor amount of zircon occurs in most samples. Only minor changes, around 15 °C, exists if pressure variations (i.e., from 2.4 to 2.8 GPa) and silica polymorph transition (α-quartz to coesite) are considering[34]. More scattered values were provided, by the calibrations of refs. [56,130,131], within the ranges of 50–100 °C in temperature difference (Supplementary Data 5).

Temperature was also evaluated for quartz crystallization specifically in HT eclogites, using Ti-in-quartz thermometers of refs. [132,133]. The activity of TiO$_2$ is set to unity (because of the widely present of Ti-rich phases) for the calibration of ref. [132] with a peak pressure value of 2.7 GPa. Considering the apparent changes in Ti-in-quartz solubility behavior that occurs at 2.0 GPa, extrapolating the calibration to higher pressures could yield inaccurate estimates of P-T conditions of crystallization[132]. Yet, the P-T estimate, if combined with Zr-in-rutile thermometer, is broadly consistent with that derived from thermodynamic modeling (within 50 °C, 0.1 GPa, Fig. 2e). In contrast, a relatively lower value (~70 °C) is given by the calibration of ref. [133], without

taking into account of the effects of pressure and TiO_2 activity (Supplementary Data 6).

Thermodynamic modeling. Pseudosection modeling for both HT and LT eclogites (AT54 and AT47, Supplementary Figs. 8, 9) were performed in the system NMnCKFMASHTO. TiO_2 was considered due to the presence of rutile/ilmenite/titanite in matrix or as inclusions in garnet porphyroblasts. The fluid phase is assumed to be pure H_2O and was set according to its exact amount in XRF data and effective bulk-rock compositions. CO_2 was neglected as only small amounts of carbonate occur as thin secondary veins. Fe_2O_3 was set according to the bulk-rock data (Supplementary Data 3). To take into account the sequestration of elements induced by the growth zoning of garnet porphyroblast, effective bulk compositions (EBCs) were adjusted from XRF compositions by removing part of the garnet modal abundance, following the quantitative method of ref. [134] derived by the Mn zoning of garnet and calculated modal garnet trendline for each major element (Supplementary Fig. 10).

The P-T pseudosections were calculated using the software Perple_X 6.87[135,136] and an internally consistent thermodynamic dataset (hp62ver.dat)[137] based on the effective recalculated bulk-rock compositions. Mineral solid-solution models are Gt(HP)[138] for garnet, Omph(GHP)[139] for omphacite, Amph (DP)[140] for amphibole, Mica(CHA)[141] for white mica, Chl(HP)[142], Ep(HP)[138] for epidote/clinozoisite, Opx (W)[143] for orthopyroxene, Bi (W)[143] for biotite, melt(G)[144] for silicate melt, Ilm (WPH)[145] for ilmenite, Pl(I1, HP)[146] for ternary-feldspar and H_2O-CO_2 fluid solution model is from ref. [147]. The pseudosections are dominated by tri- and quadri-variant fields with a few di- and quini-variant fields. P-T conditions were further constrained by comparing predicted isopleths (Phengite Si^{4+}, $X_{jadeite}$, X_{pyrope}, and $X_{grossular}$) with measured mineral compositions incorporating typical uncertainties on EMPA analyses (ca. 3% to 5%)[148].

Data availability

References

1. O'Neill, C., Jellinek, A. M. & Lenardic, A. Conditions for the onset of plate tectonics on terrestrial planets and moons. *Earth Planet. Sci. Lett.* **261**, 20–32 (2007).
2. Canfield, D. E. The evolution of the Earth surface sulfur reservoir. *Am. J. Sci.* **304**, 839–861 (2004).
3. O'Nions, R. K. & Oxburgh, E. R. Heat and helium in the earth. *Nature* **306**, 429–431 (1983).
4. Behn, M. D., Kelemen, P. B., Hirth, G., Hacker, B. R. & Massonne, H. J. Diapirs as the source of the sediment signature in arc lavas. *Nat. Geosci.* **4**, 641–646 (2011).
5. Marschall, H. R. & Schumacher, J. C. Arc magmas sourced from mélange diapirs in subduction zones. *Nat. Geosci.* **5**, 862–867 (2012).
6. Castro, A. et al. Melting relations of MORB-sediment mélanges in underplated mantle wedge plumes; implications for the origin of Cordilleran-type batholiths. *J. Petrol.* **51**, 1267–1295 (2010).
7. Skora, S. & Blundy, J. High-pressure hydrous phase relations of radiolarian clay and implications for the involvement of subducted sediment in arc magmatism. *J. Petrol.* **51**, 2211–2243 (2010).
8. Raymond, L. A. Perspectives on the roles of melanges in subduction accretionary complexes: a review. *Gondwana Res.* **74**, 68–89 (2019).
9. Cruz-Uribe, A. M., Marschall, H. R., Gaetani, G. A. & Le Roux, V. Generation of alkaline magmas in subduction zones by partial melting of mélange diapirs-an experimental study. *Geology* **46**, 343–346 (2018).
10. Beinlich, A. et al. Instantaneous rock transformations in the deep crust driven by reactive fluid flow. *Nat. Geosci.* **13**, 307–311 (2020).
11. Ganzhorn, A. C. C., Pilorgé, H. & Reynard, B. Porosity of metamorphic rocks and fluid migration within subduction interfaces. *Earth Planet. Sci. Lett.* **522**, 107–117 (2019).
12. Gorman, P. J., Kerrick, D. M. & Connolly, J. A. D. Modeling open system metamorphic decarbonation of subducting slabs. *Geochem. Geophys. Geosyst.* **7**, 1–21 (2006).
13. Herzberg, C., Condie, K. & Korenaga, J. Thermal history of the Earth and its petrological expression. *Earth Planet. Sci. Lett.* **292**, 79–88 (2010).
14. Kelemen, P. B. & Manning, C. E. Reevaluating carbon fluxes in subduction zones, what goes down, mostly comes up. *Proc. Natl Acad. Sci. USA* **112**, E3997–E4006 (2015).
15. Kessel, R., Schmidt, M. W., Ulmer, P. & Pettke, T. Trace element signature of subduction-zone fluids, melts and supercritical liquids at 120-180 km depth. *Nature* **437**, 724–727 (2005).
16. Hermann, J. & Rubatto, D. Accessory phase control on the trace element signature of sediment melts in subduction zones. *Chem. Geol.* **265**, 512–526 (2009).
17. Schmidt, M. W. & Poli, S. *Devolatilization During Subduction. Treatise on Geochemistry* 2nd edn, Vol. 4 (Elsevier Ltd., 2013).
18. Bebout, G. E. Metamorphic chemical geodynamics of subduction zones. *Earth Planet. Sci. Lett.* **260**, 373–393 (2007).
19. Nielsen, S. G. & Marschall, H. R. Geochemical evidence for mélange melting in global arcs. *Sci. Adv.* **3**, e1602402 (2017).
20. Codillo, E. A., Le Roux, V. & Marschall, H. R. Arc-like magmas generated by mélange-peridotite interaction in the mantle wedge. *Nat. Commun.* **9**, 2864 (2018).
21. Hall, P. S. & Kincaid, C. Diapiric flow at subduction zones: a recipe for rapid transport. *Science* **292**, 2472–2475 (2001).
22. Gerya, T. V., Connolly, J. A. D., Yuen, D. A., Gorczyk, W. & Capel, A. M. Seismic implications of mantle wedge plumes. *Phys. Earth Planet. Inter.* **156**, 59–74 (2006).
23. Gerya, T. V. & Yuen, D. A. Rayleigh - Taylor instabilities from hydration and melting propel 'cold plumes' at subduction zones. *Earth Planet. Sci. Lett.* **212**, 47–62 (2003).
24. Castro, J. M. et al. Timescales of spherulite crystallization in obsidian inferred from water concentration profiles. *Am. Mineral.* **93**, 1816–1822 (2008).
25. Zhu, G. et al. Three-dimensional dynamics of hydrous thermal-chemical plumes in oceanic subduction zones. *Geochem. Geophys. Geosyst.* **10**, 1–20 (2009).
26. Bebout, G. E. & Barton, M. D. Tectonic and metasomatic mixing in a high-T, subduction-zone mélange - insights into the geochemical evolution of the slab-mantle interface. *Chem. Geol.* **187**, 79–106 (2002).
27. Abers, G. A. Hydrated subducted crust at 100-250 km depth. *Earth Planet. Sci. Lett.* **176**, 323–330 (2000).
28. King, R. L., Bebout, G. E., Moriguti, T. & Nakamura, E. Elemental mixing systematics and Sr-Nd isotope geochemistry of mélange formation: obstacles to identification of fluid sources to arc volcanics. *Earth Planet. Sci. Lett.* **246**, 288–304 (2006).
29. Bebout, G. E. & Penniston-Dorland, S. C. Fluid and mass transfer at subduction interfaces-the field metamorphic record. *Lithos* **240–243**, 228–258 (2016).
30. Agard, P., Yamato, P., Jolivet, L. & Burov, E. Exhumation of oceanic blueschists and eclogites in subduction zones: timing and mechanisms. *Earth-Sci. Rev.* **92**, 53–79 (2009).
31. John, T. et al. Subducted seamounts in an eclogite-facies ophiolite sequence: the Andean Raspas Complex, SW Ecuador. *Contrib. Mineral. Petrol.* **159**, 265–284 (2010).
32. Bayet, L., John, T., Agard, P., Gao, J. & Li, J. L. Massive sediment accretion at ~80 km depth along the subduction interface: evidence from the southern Chinese Tianshan. *Geology* **46**, 495–498 (2018).
33. Tan, Z. et al. Architecture and P-T-deformation-time evolution of the Chinese SW-Tianshan HP/UHP complex: implications for subduction dynamics. *Earth-Sci. Rev.* **197**, 102894 (2019).
34. Tan, Z., Agard, P., Gao, J., Hong, T. & Wan, B. Concordant pulse in Mn, Y and HREEs concentrations during UHP eclogitic garnet growth: transient rock dynamics along a cold subduction plate interface. *Earth Planet. Sci. Lett.* **530**, 115908 (2020).
35. Tan, Z. et al. P–T–time-isotopic evolution of coesite-bearing eclogites: implications for exhumation processes in SW Tianshan. *Lithos* **278–281**, 1–25 (2017).
36. Tan, Z., Gao, J., Jiang, T., Wang, X. & Zhang, X. P–T–time (phengite Ar closure) history of spatially close-outcropping HP and UHP oceanic eclogites

(southwestern Tianshan): implication for a potential deep juxtaposing process during exhumation? *Int. Geol. Rev.* **61**, 1270–1293 (2018).

37. Tan, Z. et al. Final closure of the Paleo Asian Ocean basin in the early Triassic. *Commun. Earth Environ.* **3**, 1–15 (2022).

38. Yang, X., Zhang, L., Tian, Z. & Bader, T. Petrology and U-Pb zircon dating of coesite-bearing metapelite from the Kebuerte Valley, Western Tianshan, China. *J. Asian Earth Sci.* **70–71**, 295–307 (2013).

39. Li, J. L., Gao, J., John, T., Klemd, R. & Su, W. Fluid-mediated metal transport in subduction zones and its link to arc-related giant ore deposits: Constraints from a sulfide-bearing HP vein in lawsonite eclogite (Tianshan, China). *Geochim. Cosmochim. Acta* **120**, 326–362 (2013).

40. Zhang, L., Wang, Y., Zhang, L. & Lü, Z. Ultrahigh pressure metamorphism and tectonic evolution of southwestern tianshan orogenic belt, China: A comprehensive review. *Geol. Soc. Spec. Publ.* **474**, 133–152 (2019).

41. Şengör, A. M. C., Sunal, G., Natal'in, B. A. & van der Voo, R. The Altaids: a review of twenty-five years of knowledge accumulation. *Earth-Sci. Rev.* **228**, 104013 (2022).

42. Xiao, W. et al. A tale of amalgamation of three Permo-Triassic collage systems in Central Asia: oroclines, sutures, and terminal accretion. *Annu. Rev. Earth Planet. Sci.* **43**, 477–507 (2015).

43. Xiao, W., Windley, B. F., Allen, M. B. & Han, C. Paleozoic multiple accretionary and collisional tectonics of the Chinese Tianshan orogenic collage. *Gondwana Res.* **23**, 1316–1341 (2013).

44. Charvet, J. et al. Palaeozoic tectonic evolution of the Tianshan belt, NW China. *Sci. China Earth Sci.* **54**, 166–184 (2011).

45. Alexeiev, D. V. et al. Tectono stratigraphic framework and Palaeozoic evolution of the Chinese South Tianshan 1. *Geotectonics* **2**, 3–35 (2015).

46. Wang, X. et al. Final assembly of the southwestern Central Asian Orogenic Belt as constrained by the evolution of the South Tianshan Orogen: links With Gondwana and Pangea. *J. Geophys. Res. Solid Earth* **123**, 7361–7388 (2018).

47. Xiao, W., Zhang, L. C., Qin, K. Z., Sun, S. & Li, J. L. Paleozoic accretionary and collisional tectonics of the Eastern Tianshan (China): Implications for the continental growth of central Asia. *Am. J. Sci.* **304**, 370–395 (2004).

48. Loury, C., Rolland, Y., Cenki-Tok, B., Lanari, P. & Guillot, S. Late Paleozoic evolution of the South Tien Shan: insights from P-T estimates and allanite geochronology on retrogressed eclogites (Chatkal range, Kyrgyzstan). *J. Geodyn.* **96**, 62–80 (2016).

49. Mühlberg, M. et al. Late carboniferous high-pressure metamorphism of the Kassan Metamorphic Complex (Kyrgyz Tianshan) and assembly of the SW Central Asian Orogenic Belt. *Lithos* **264**, 41–55 (2016).

50. Volkova, N. I. & Budanov, V. I. Geochemical discrimination of metabasalt rocks of the Fan-Karategin transitional blueschist/greenschist belt, South Tianshan, Tajikistan: Seamount volcanism and accretionary tectonics. *Lithos* **47**, 201–216 (1999).

51. Loury, C. et al. Tectonometamorphic evolution of the Atbashi high-P units (Kyrgyz CAOB, Tien Shan): implications for the closure of the Turkestan Ocean and continental subduction–exhumation of the South Kazakh continental margin. *J. Metamorph. Geol.* **36**, 959–985 (2018).

52. Sang, M., Xiao, W. & Windley, B. F. Unravelling a Devonian–Triassic seamount chain in the South Tianshan high-pressure/ultrahigh-pressure accretionary complex in the Atbashi area (Kyrgyzstan). *Geol. J.* https://doi.org/10.1002/gj.3776 (2020).

53. Sang, M. et al. Structural styles and zircon ages of the South Tianshan accretionary complex, Atbashi Ridge, Kyrgyzstan: insights for the anatomy of ocean plate stratigraphy and accretionary processes. *J. Asian Earth Sci.* **153**, 9–41 (2018).

54. Sang, M., Xiao, W., Feng, Q. & Windley, B. F. Radiolarian age and geochemistry of cherts from the Atbashi accretionary complex, Kyrgyz South Tianshan. *Geol. J.* https://doi.org/10.1002/gj.3952 (2020).

55. Holness, M. B., Cesare, B. & Sawyer, E. W. Melted rocks under the microscope: microstructures and their interpretation. *Elements* **7**, 247–252 (2011).

56. Zack, T., Moraes, R. & Kronz, A. Temperature dependence of Zr in rutile: empirical calibration of a rutile thermometer. *Contrib. Mineral. Petrol.* **148**, 471–488 (2004).

57. Tomkins, H. S., Powell, R. & Ellis, D. J. The pressure dependence of the zirconium-in-rutile thermometer. *J. Metamorph. Geol.* **25**, 703–713 (2007).

58. Guillot, S., Hattori, K., Agard, P., Schwartz, S. & Vidal, O. Exhumation processes in oceanic and continental subduction contexts: a review. In *Subduction Zone Geodynamics* 175–205 (Springer, 2009). https://doi.org/10.1007/978-3-540-87974-9_10.

59. Williams, I. S. U-Th-Pb Geochronology by Ion Microprobe ABOUT TIME. *Rev. Econ. Geol.* **7**, 1–35 (1998).

60. Hoskin, P. W. O. & Schaltegger, U. The composition of zircon and igneous and metamorphic petrogenesis. *Rev. Mineral. Geochem.* **53**, 27–62 (2003).

61. Gao, L., Xiao, W., Tan, Z., Wang, X. & Guo, Y. A newly defined, long-lived Paleozoic intra-oceanic arc in the South Tianshan (NW China): Implications for multiple accretionary tectonics in the southern Altaids. *GSA Bull.* 1–20 https://doi.org/10.1130/b36355.1 (2022).

62. Liu, X. et al. The youngest Permian Ocean in Central Asian Orogenic Belt: evidence from geochronology and geochemistry of Bingdaban Ophiolitic Mélange in Central Tianshan, northwestern China. *Geol. J.* **55**, 2062–2079 (2020).

63. Pearce, J. Tectonic implications of the composition of volcanic arc magmas. *Annu. Rev. Earth Planet. Sci.* **23**, 251–285 (1995).

64. McCulloch, M. T. & Gamble, J. A. Geochemical and geodynamical constraints on subduction zone magmatism. *Earth Planet. Sci. Lett.* **102**, 358–374 (1991).

65. Wang, K. et al. Diapir melting of subducted mélange generating alkaline arc magmatism and its implications for material recycling at subduction zone settings. *Geophys. Res. Lett.* **49**, 1–13 (2022).

66. Workman, R. K. & Hart, S. R. Major and trace element composition of the depleted MORB mantle (DMM). *Earth Planet. Sci. Lett.* **231**, 53–72 (2005).

67. Staudigel, H., Plank, T., White, B. & Schmincke, H. U. Geochemical fluxes during seafloor alteration of the basaltic upper oceanic crust: DSDP sites 417 and 418. *Geophys. Monogr. Ser.* **96**, 19–38 (1996).

68. Gale, A., Dalton, C. A., Langmuir, C. H., Su, Y. & Schilling, J. G. The mean composition of ocean ridge basalts. *Geochem. Geophys. Geosyst.* **14**, 489–518 (2013).

69. Elliott, T., Plank, T., Zindler, A., White, W. & Bourdon, B. Element transport from slab to volcanic front at the Mariana arc. *J. Geophys. Res. Solid Earth* **102**, 14991–15019 (1997).

70. Kelemen, P. B., Yogodzinski, G. M. & Scholl, D. W. Along-strike variation in lavas of the Aleutian island arc: implications for the genesis of high Mg# andesite and the continental crust. *Inside Subduction Fact. Geophys. Monogr.* **138**, 223–276 (2003).

71. Nielsen, S. G. et al. Tracking along-arc sediment inputs to the Aleutian arc using thallium isotopes. *Geochim. Cosmochim. Acta* **181**, 217–237 (2016).

72. Miller, D. P., Marschall, H. R. & Schumacher, J. C. Metasomatic formation and petrology of blueschist-facies hybrid rocks from Syros (Greece): implications for reactions at the slab-mantle interface. *Lithos* **107**, 53–67 (2009).

73. Enami, M., Liou, J. G. & Mattinson, C. G. Epidote minerals in high P/T metamorphic terranes: subduction zone and high- to ultrahigh-pressure metamorphism. *Rev. Mineral. Geochem.* **56**, 347–398 (2004).

74. Bayet, L. et al. Tectonic evolution of the Tianshan Akeyazi metamorphic complex (NW China). *Lithos* **354–355**, 105273 (2018).

75. Xia, B., Brown, M. & Lifie, Z. P–T evolution and tectonic significance of lawsonite-bearing schists from the eastern segment of the southwestern Tianshan, China. *J. Metamorph. Geol.* https://doi.org/10.1111/jmg.12555 (2020).

76. Du, J. X., Zhang, L. F., Bader, T., Chen, Z. Y. & Lü, Z. Metamorphic evolution of relict lawsonite-bearing eclogites from the (U) HP metamorphic belt in the Chinese southwestern Tianshan. *J. Metamorph. Geol.* **32**, 575–598 (2014).

77. Lü, Z., Zhang, L., Yue, J. & Li, X. Ultrahigh-pressure and high-P lawsonite eclogites in Muzhaerte, Chinese western Tianshan. *J. Metamorph. Geol.* **37**, 717–743 (2019).

78. Lü, Z., Zhang, L., Du, J. & Bucher, K. Petrology of coesite-bearing eclogite from Habutengsu Valley, western Tianshan, NW China and its tectonometamorphic implication. *J. Metamorph. Geol.* **27**, 773–787 (2009).

79. Agard, P., Plunder, A., Angiboust, S., Bonnet, G. & Ruh, J. The subduction plate interface: rock record and mechanical coupling (from long to short timescales). *Lithos* **320–321**, 537–566 (2018).

80. Penniston-Dorland, S. C., Kohn, M. J. & Manning, C. E. The global range of subduction zone thermal structures from exhumed blueschists and eclogites: rocks are hotter than models. *Earth Planet. Sci. Lett.* **428**, 243–254 (2015).

81. Peacock, S. M. Thermal effects of metamorphic fluids in subduction zones. *Geology* **15**, 1057–1060 (1987).

82. Royden, L. H. The steady state thermal structure of eroding orogenic belts and accretionary prisms. *J. Geophys. Res.* **98**, 4487–4507 (1993).

83. Kohn, M. J., Castro, A. E., Kerswell, B. C., Ranero, C. R. & Spear, F. S. Shear heating reconciles thermal models with the metamorphic rock record of subduction. *Proc. Natl Acad. Sci. USA* **115**, 11706–11711 (2018).

84. Gerya, T. V., Stöckhert, B. & Perchuk, A. L. Exhumation of high-pressure metamorphic rocks in a subduction channel: a numerical simulation. *Tectonics* **21**, 6-1-6–19 (2002).

85. Blanco-Quintero, I. F., García-Casco, A. & Gerya, T. V. Tectonic blocks in serpentinite mélange (Eastern Cuba) reveal large-scale convective flow of the subduction channel. *Geology* **39**, 79–82 (2011).

86. Stachnik, J. C., Abers, G. A. & Christensen, D. H. Seismic attenuation and mantle wedge temperatures in the Alaska subduction zone. *J. Geophys. Res. Solid Earth* **109**, 1–17 (2004).

87. Takanami, T., Selwyn Sacks, I. & Hasegawa, A. Attenuation structure beneath the volcanic front in northeastern Japan from broad-band seismograms. *Phys. Earth Planet. Inter.* **121**, 339–357 (2000).

88. Abers, G. A., van Keken, P. E., Kneller, E. A., Ferris, A. & Stachnik, J. C. The thermal structure of subduction zones constrained by seismic imaging: implications for slab dehydration and wedge flow. *Earth Planet. Sci. Lett.* **241**, 387–397 (2006).

89. Syracuse, E. M. et al. The global range of subduction zone thermal models. *Phys. Earth Planet. Inter.* **183**, 73–90 (2010).

90. van der Straaten, F., Schenk, V., John, T. & Gao, J. Blueschist-facies rehydration of eclogites (Tian Shan, NW-China): implications for fluid-rock interaction in the subduction channel. *Chem. Geol.* **255**, 195–219 (2008).

91. Li, J. L., Klemd, R., Gao, J. & John, T. Poly-cyclic metamorphic evolution of eclogite: evidence for multistage burial-exhumation cycling in a subduction channel. *J. Petrol.* **57**, 119–146 (2016).

92. Hawkesworth, C. J., Gallagher, K., Hergt, J. M. & McDermott, F. Mantle and slab contribution in arc magmas. *Annu. Rev. Earth Planet. Sci.* **21**, 175–204 (1993).

93. Abers, G. A. Seismic low-velocity layer at the top of subducting slabs: observations, predictions, and systematics. *Phys. Earth Planet. Inter.* **149**, 7–29 (2005).

94. Schwarzenbach, E. et al. On exhumation velocities of high-pressure units based on insights from chemical zonations in garnet (Tianshan, NW China). *Earth Planet. Sci. Lett.* **570**, 117065 (2021).

95. Xiao, W. et al. Late Paleozoic to early Triassic multiple roll-back and oroclinal bending of the Mongolia collage in Central Asia. *Earth-Sci. Rev.* **186**, 94–128 (2018).

96. Tang, G. J. et al. Short episodes of crust generation during protracted accretionary processes: Evidence from Central Asian Orogenic Belt, NW China. *Earth Planet. Sci. Lett.* **464**, 142–154 (2017).

97. Chapman, J. B. & Ducea, M. N. The role of arc migration in Cordilleran orogenic cyclicity. *Geology* **47**, 627–631 (2019).

98. Chen, C., Lee, C.-T. A., Tang, M., Biddle, K. & Sun, W. Lithium systematics in global arc magmas and the importance of crustal thickening for lithium enrichment. *Nat. Commun.* **11**, 5313 (2020).

99. Van Keken, P. E., Hacker, B. R., Syracuse, E. M. & Abers, G. A. Subduction factory: 4. Depth-dependent flux of H2O from subducting slabs worldwide. *J. Geophys. Res. Solid Earth* **116**, B01401 (2011).

100. Stewart, E. M. & Ague, J. J. Pervasive subduction zone devolatilization recycles CO2 into the forearc. *Nat. Commun.* **11**, 1–8 (2020).

101. Abbott, D., Burgess, L., Longhi, J. & Smith, W. H. F. An empirical thermal history of the Earth's upper mantle. *J. Geophys. Res.* **99**, 835–850 (1994).

102. Plank, T. *The Chemical Composition of Subducting Sediments. Treatise on Geochemistry*: 2nd edn, Vol. 4 (Elsevier Ltd., 2013).

103. Johnson, M. C. & Plank, T. Dehydration and melting experiments constrain the fate of subducted sediments. *Geochem. Geophys. Geosyst.* **1**, 1007 (2000).

104. Evans, K. A. The redox budget of subduction zones. *Earth-Sci. Rev.* **113**, 11–32 (2012).

105. Defant, M. J. & Drummond, M. S. Derivation of some modern arc magmas by melting of young subducted lithosphere. *Nature* **347**, 662–665 (1990).

106. Wang, C., Liang, Y., Dygert, N. & Xu, W. Formation of orthopyroxenite by reaction between peridotite and hydrous basaltic melt: an experimental study. *Contrib. Mineral. Petrol.* **171**, 1–18 (2016).

107. Kelemen, P. B., Dick, H. J. B. & Quick, J. E. Formation of harzburgite by pervasive melt/rock reaction in the upper mantle. *Nature* **358**, 635–641 (1992).

108. Le Roux, V., Dick, H. J. B. & Shimizu, N. Tracking flux melting and melt percolation in supra-subduction peridotites (Josephine ophiolite, USA). *Contrib. to Mineral. Petrol.* **168**, 1–22 (2014).

109. Jean, M. M., Shervais, J. W., Choi, S. H. & Mukasa, S. B. Melt extraction and melt refertilization in mantle peridotite of the Coast Range ophiolite: an LA-ICP-MS study. *Contrib. Mineral. Petrol.* **159**, 113–136 (2010).

110. Malaspina, N., Hermann, J., Scambelluri, M. & Compagnoni, R. Polyphase inclusions in garnet-orthopyroxenite (Dabie Shan, China) as monitors for metasomatism and fluid-related trace element transfer in subduction zone peridotite. *Earth Planet. Sci. Lett.* **249**, 173–187 (2006).

111. Elliott, T. Tracers of the slab. *Geophys. Monogr. Ser.* **138**, 23–45 (2004).

112. Morris, J. & Tera, F. 10Be and 9Be in mineral separates and whole rocks from volcanic arcs: Implications for sediment subduction. *Geochim. Cosmochim. Acta* **53**, 3197–3206 (1989).

113. John, T., Scherer, E. E., Haase, K. & Schenk, V. Trace element fractionation during fluid-induced eclogitization in a subducting slab: trace element and Lu-Hf-Sm-Nd isotope systematics. *Earth Planet. Sci. Lett.* **227**, 441–456 (2004).

114. John, T., Klemd, R., Gao, J. & Garbe-Schönberg, C. D. Trace-element mobilization in slabs due to non steady-state fluid-rock interaction: constraints from an eclogite-facies transport vein in blueschist (Tianshan, China). *Lithos* **103**, 1–24 (2008).

115. Tao, R., Zhang, L., Li, S., Zhu, J. & Ke, S. Significant contrast in the Mg-C-O isotopes of carbonate between carbonated eclogite and marble from the S.W. Tianshan UHP subduction zone: evidence for two sources of recycled carbon. *Chem. Geol.* **483**, 65–77 (2018).

116. Zhu, J., Zhang, L., Tao, R. & Fei, Y. The formation of graphite-rich eclogite vein in S.W. Tianshan (China) and its implication for deep carbon cycling in subduction zone. *Chem. Geol.* **533**, 119430 (2020).

117. Hu, H. et al. Retrograde carbon sequestration in orogenic complexes: a case study from the Chinese southwestern Tianshan. *Lithos* **392–393**, 106151 (2021).

118. Peng, W. et al. Multistage CO2 sequestration in the subduction zone: Insights from exhumed carbonated serpentinites, SW Tianshan UHP belt, China. *Geochim. Cosmochim. Acta* **270**, 218–243 (2020).

119. Xue, D., Wang, H., Liu, Y., Xie, L. & Shen, P. An improved procedure for the determination of ferrous iron mass fraction in silicate rocks using a Schlenk Line-based digestion apparatus to exclude oxygen. *Geostand. Geoanal. Res.* **41**, 411–425 (2017).

120. Weis, D. et al. High-precision isotopic characterization of USGS reference materials by TIMS and MC-ICP-MS. *Geochem. Geophys. Geosyst.* **7**, Q08006 (2006).

121. Paton, C. et al. Improved laser ablation U-Pb zircon geochronology through robust downhole fractionation correction. *Geochem. Geophys. Geosyst.* **11**, Q0AA06 (2010).

122. Van Achterbergh, E, Ryan, C. G & Griffin, W. L. GLITTER: on-line interactive data reduction for the laser ablation inductively coupled plasma mass spectrometry microprobe. Geochemical Society. In *Ninth Annual VM Goldschmidt Conference* Vol. 1, 7215 (1999).

123. Zong, K. et al. The assembly of Rodinia: the correlation of early Neoproterozoic (ca. 900 Ma) high-grade metamorphism and continental arc formation in the southern Beishan Orogen, southern Central Asian Orogenic Belt (CAOB). *Precambrian Res.* **290**, 32–48 (2017).

124. Hu, Z. et al. 'Wave' signal-smoothing and mercury-removing device for laser ablation quadrupole and multiple collector ICPMS analysis: application to lead isotope analysis. *Anal. Chem.* **87**, 1152–1157 (2015).

125. Liu, Y. et al. Continental and oceanic crust recycling-induced melt-peridotite interactions in the Trans-North China Orogen: U-Pb dating, Hf isotopes and trace elements in zircons from mantle xenoliths. *J. Petrol.* **51**, 537–571 (2009).

126. Ludwig, K. R. A Geochronological Toolkit for Microsoft Excel No. 4. 71 (Berkeley Geochronol. Center, Spec. Publ., 2003).

127. Luvizotto, G. L. et al. Rutile crystals as potential trace element and isotope mineral standards for microanalysis. *Chem. Geol.* **261**, 346–369 (2009).

128. Li, Q. et al. A high precision U-Pb age of metamorphic rutile in coesite-bearing eclogite from the Dabie Mountains in central China: a new constraint on the cooling history. *Chem. Geol.* **200**, 255–265 (2003).

129. Li, Q. L. et al. SIMS U-Pb rutile age of low-temperature eclogites from southwestern Chinese Tianshan, NW China. *Lithos* **122**, 76–86 (2011).

130. Watson, E. B., Wark, D. A. & Thomas, J. B. Crystallization thermometers for zircon and rutile. *Contrib. Mineral. Petrol.* **151**, 413–433 (2006).

131. Ferry, J. M. & Watson, E. B. New thermodynamic models and revised calibrations for the Ti-in-zircon and Zr-in-rutile thermometers. *Contrib. Mineral. Petrol.* **154**, 429–437 (2007).

132. Thomas, J. B. et al. TitaniQ under pressure: the effect of pressure and temperature on the solubility of Ti in quartz. *Contrib. Mineral. Petrol.* **160**, 743–759 (2010).

133. Wark, D. A. & Watson, E. B. TitaniQ: a titanium-in-quartz geothermometer. *Contrib. Mineral. Petrol.* **152**, 743–754 (2006).

134. Evans, T. P. A method for calculating effective bulk composition modification due to crystal fractionation in garnet-bearing schist: Implications for isopleth thermobarometry. *J. Metamorph. Geol.* **22**, 547–557 (2004).

135. Connolly, J. A. D. Multivariable phase diagrams: an algorithm based on generalized thermodynamics. *Am. J. Sci.* **290**, 666–718 (1990).

136. Connolly, J. A. D. Computation of phase equilibria by linear programming: a tool for geodynamic modeling and its application to subduction zone decarbonation. *Earth Planet. Sci. Lett.* **236**, 524–541 (2005).

137. Holland, T. J. B. & Powell, R. An improved and extended internally consistent thermodynamic dataset for phases of petrological interest, involving a new equation of state for solids. *J. Metamorph. Geol.* **29**, 333–383 (2011).

138. Holland, T. J. B. & Powell, R. An internally consistent thermodynamic data set for phases of petrological interest. *J. Metamorph. Geol.* **16**, 309–343 (1998).

139. Green, E., Holland, T. & Powell, R. An order-disorder model for omphacitic pyroxenes in the system jadeite-diopside-hedenbergite-acmite, with applications to eclogitic rocks. *Am. Mineral.* **92**, 1181–1189 (2007).

140. Diener, J. F. A., Powell, R., White, R. W. & Holland, T. J. B. A new thermodynamic model for clino- and orthoamphiboles in the system Na2O-CaO-FeO-MgO-Al2O3-SiO2 -H2O-O. *J. Metamorph. Geol.* **25**, 631–656 (2007).

141. Coggon, R. & Holland, T. J. B. Mixing properties of phengitic micas and revised garnet-phengite thermobarometers. *J. Metamorph. Geol.* **20**, 683–696 (2002).

142. Holland, T., Baker, J. & Powell, R. Mixing properties and activity-composition relationships of chlorites in the system MgO-FeO-Al2O3-SiO2-H2O. *Eur. J. Mineral.* **10**, 395–406 (1998).

143. White, R. W., Powell, R., Holland, T. J. B., Johnson, T. E. & Green, E. C. R. New mineral activity-composition relations for thermodynamic calculations in metapelitic systems. *J. Metamorph. Geol.* **32**, 261–286 (2014).

144. Green, E. C. R. et al. Activity–composition relations for the calculation of partial melting equilibria in metabasic rocks. *J. Metamorph. Geol.* **34**, 845–869 (2016).

145. White, R. W., Powell, R. & Holland, T. J. B. Calculation of partial melting equilibria in the system. *J. Metamorph. Geol.* **19**, 139–153 (2001).

146. Holland, T. & Powell, R. Activity-compositions relations for phases in petrological calculations: an asymmetric multicomponent formulation. *Contrib. Mineral. Petrol.* **145**, 492–501 (2003).

147. Connolly, J. A. D. & Trommsdorff, V. Petrogenetic grids for metacarbonate rocks: pressure-temperature phase-diagram projection for mixed-volatile systems. *Contrib. Mineral. Petrol.* **108**, 93–105 (1991).

148. Lifshin, E. & Gauvin, R. Minimizing errors in electron microprobe analysis. *Microsc. Microanal.* **7**, 168–177 (2001).

149. Palin, R. M. et al. High-grade metamorphism and partial melting of basic and intermediate rocks. *J. Metamorph. Geol.* **34**, 871–892 (2016).

150. Thomsen, T. B. & Schmidt, M. W. Melting of carbonated pelites at 2.5-5.0 GPa, silicate-carbonatite liquid immiscibility, and potassium-carbon metasomatism of the mantle. *Earth Planet. Sci. Lett.* **267**, 17–31 (2008).

151. Hermann, J. & Spandler, C. J. Sediment melts at sub-arc depths: an experimental study. *J. Petrol.* **49**, 717–740 (2008).

152. Bohlen, S. R. & Boettcher, A. H. The quartz L/R arrows coesite transformation: a precise determination and the effects of other components. *J. Geophys. Res.* **87**, 7073–7078 (1982).

153. Li, X. P., Zhang, L. F., Wilde, S. A., Song, B. & Liu, X. M. Zircons from rodingite in the Western Tianshan serpentinite complex: mineral chemistry and U-Pb ages define nature and timing of rodingitization. *Lithos* **118**, 17–34 (2010).

154. Li, R. et al. The discovery of Carboniferous-Permian radiolarians from the upatarkan group in the western South Tianshan. *Chin. J. Geol.* **40**, 220–226 (2005).

155. Steffen, B. & Seyfried, A. Methods for measuring pedestrian density, flow, speed and direction with minimal scatter. *Phys. A Stat. Mech. Its Appl.* **389**, 1902–1910 (2010).

Author contributions
M. S., Z. T., and W. X. conceived the study. M. S. and W. X. conducted field geological exploration and sample collection. M. S., Z. T., H. W., Q. M., R. L., and Q. Q. conducted the experimental analyses and data collection. Z. T. and M. S. conducted data processing and visualizing. Z. T., M. S., W. X., Q. M., H. W., and Q. Q. contributed to the interpretation of the results and wrote the manuscript.

Competing interests
The authors declare no competing interests.

Additional information
Supplementary information The online version contains supplementary material available at https://doi.org/10.1038/s43247-023-01106-8.

Correspondence and requests for materials should be addressed to Zhou Tan or Wenjiao Xiao.

Peer review information *Communications Earth & Environment* thanks the anonymous reviewers for their contribution to the peer review of this work. Primary Handling Editor: Joe Aslin. A peer review file is available.

Reprints and permission information is available at http://www.nature.com/reprints

Publisher's note Springer Nature remains neutral with regard to jurisdictional claims in published maps and institutional affiliations.